Title
Brainstem control of neonatal vocalizations

Author
Wei, Xin Paul

Publication Date
2021

Peer reviewed|Thesis/dissertation

Brainstem control of neonatal vocalizations

by
Paul Wei

DISSERTATION
Submitted in partial satisfaction of the requirements for degree of
DOCTOR OF PHILOSOPHY

in

Biomedical Sciences

in the

GRADUATE DIVISION
of the
UNIVERSITY OF CALIFORNIA, SAN FRANCISCO

Approved:

DocuSigned by:
Robert Edwards
91579E192F544AF...

Robert Edwards
Chair

DocuSigned by:
Kevin Yackle
DocuSigned by:
David Julius
DocuSigned by:
Massimo Scanziani
4AF406E430B7472...

Kevin Yackle
David Julius
Massimo Scanziani

Committee Members

Acknowledgements

I feel so fortunate to have had Kevin Yackle as my thesis advisor and mentor. From you, I have learned so much, about neuroscience, genetics, breathing and optimism. You have always pushed me to think critically about the problem, scavenge the literature for clues and come up with the best and most definitive experiments to test a hypothesis. Most importantly, I learned to always *just do* the next experiment, because only by doing it, will you know if it works! My favorite moments in the last five years have been sitting around the whiteboard window with you, with an Expo marker, drawing out our data, brainstorming models, and coming up with the next sets of experiment. Your enthusiasm and excitement for science is truly infectious and your unwavering support have helped propel me past the largest obstacles and setbacks. For that, I am eternally grateful.

I want to give my most heartfelt thanks to my co-mentor David Julius. Thank you for generously adopting me as an honorary member of your lab. Your insightful suggestions, pointed questions, and clear focus on the big picture, helped to shape me into a rigorous, thoughtful, and curious scientist. Your anecdotes often brought levity to my day, and your vast experiences reminded me that I'm never alone. Your willingness to always lend a hand at a moment's notice, whether it's editing my manuscript or opening the liquid nitrogen tank, showed your dedication to your trainees. Thank you for being a guiding light for me throughout my graduate training.

I would also like to thank members of my thesis committee, Robert Edwards and Massimo Scanziani, for your insightful guidance through the many twists and turns in the project. You never let me lose sight of the goal and always pushed me towards the most interesting questions and

valuable experiments. You were able to see flaws in the data that I overlooked but also grasp the significance of the conclusions I may have been too immersed to realize. Your sage advice, continuous guidance and enthusiastic support helped keep me on track.

Science is a team sport, and members of the Yackle and Julius labs have been the best teammates and colleagues one could ask for. In particular, I want to acknowledge my co-author and friend Matt Collie, whom I shared the electrophysiology room with for two years, working side by side every day to figure out the electrophysiological mechanisms driving the mysterious brainstem pacemaker oscillator which, at the time, had unknown function. And to Iris Bachmutsky, whom I had the fortune of working with on multiple projects – your drive to try new experiments and techniques is truly inspirational. To the other brilliant members of the Yackle and Julius labs, from whom I learned so much every day, not only from your expertise in physiology, sensory biology, cell biology and structure biology, but more importantly, on *how* to do science. Thank you for your guidance and friendship.

This project would not have been possible without the conceptual and experimental support from our wonderful collaborators in France, Gilles Fortin and Bowen Dempsey. I am grateful for your generosity in hosting me in Gif-sur-Yvette, as we tirelessly worked on an experiment that would change the trajectory of this project.

I am also very appreciative of the unwavering support from the Medical Scientist Training Program and the Biomedical Sciences program, in particular, from Mark Anderson, Geri Ehle, Aimee Kao, Dean Sheppard, and Demian Sainz. I am also indebted to my friends in the program,

in particular my former roommates, Ian Boothby and Kun Leng, who have made this long journey not only doable, but fun.

Lastly, I would like to thank my life partner Monica Chao, and my parents, Liping Chen and Qi Wei, for always being by my side every step of the way. None of this would be possible without your unconditional love and support. I dedicate this dissertation to you.

Contributions

Chapter 2 of this dissertation is modified from:

Wei, X.P., Collie, M., Dempsey, B., Fortin, G., Yackle, K. (2021). A novel reticular oscillator in the brainstem synchronizes neonatal crying with breathing. bioRxiv 2021.02.26.433060; doi: https://doi.org/10.1101/2021.02.26.433060

audentis Fortuna iuvat

Fortune favors the bold

- Virgil, *Aeneid*

Abstract

Brainstem control of neonatal vocalizations

by

Xin Paul Wei

Human speech can be divided into short, rhythmically-timed elements, similar to syllables within words. Even our cries and laughs, as well as the vocalizations of other species, are periodic. However, the cellular and molecular mechanisms underlying the tempo of mammalian vocalizations remain unknown. Furthermore, even the core cells that produce vocalizations remain ill-defined. Here we describe rhythmically-timed neonatal mouse vocalizations that occur within single breaths, and identify a brainstem node that is necessary for and sufficient to structure these cries, which we name the intermediate reticular oscillator (iRO). We show that the iRO acts autonomously and sends direct inputs to key muscles and the respiratory rhythm generator in order to coordinate neonatal vocalizations with breathing, as well as paces and patterns these cries. These results reveal that a novel mammalian brainstem oscillator embedded within the conserved breathing circuitry plays a central role in the production of neonatal vocalizations.

Table of Contents

List of Figures

List of Tables

List of Abbreviations

ACSF	artificial cerebral spinal fluid
BötC	Bötzinger Complex
Cbx	carbenoxolone
cNA	compact nucleus ambiguus
CNXII	cranial nerve 12, hypoglossal nerve
CT	cricothyroid muscle
CTB	cholera toxin subunit B
CPG	central pattern generator
EMG	electromyography
EPSC/EPSP	excitatory post-synaptic current/potential
GG	genioglossus muscle
I_{NaP}	persistent sodium current
IPSC/IPSP	inhibitory post-synaptic current/potential
iRO	intermediate reticular oscillator
KF	Kölliker-Fuse nucleus
LTCC	L-type calcium channel
NTS	nucleus tractus solitarius
PAG	periaqueductal gray
PBN	parabrachial nucleus
PiCo	post inspiratory complex
preBötC	preBötzinger complex
RAm	retroambiguus
RTN/pFRG	retrotrapezoid nucleus/parafacial respiratory group
rv-iRF	rostral ventral intermediate reticular formation
TA	thyroarytenoid muscle
USV	ultrasonic vocalization
VIRT	ventral intermediate reticular tract

CHAPTER 1: INTRODUCTION

The brainstem is the critical center of life, maintaining vital physiological functions such as the control of breathing, the cardiovascular system and sleep. Of the autonomic behaviors controlled by the brainstem, a subset of them, including breathing, chewing, and swallowing, involve finely coordinated rhythmic motor tasks. These behaviors are controlled by a special type of neural circuit known as a central pattern generator (CPG) (Marder and Bucher, 2001).

CENTRAL PATTERN GENERATORS

Central pattern generators are small, self-contained networks of neurons that pattern rhythmic motor activity. CPGs in vertebrates primarily reside in the brainstem and spinal cord, and each CPG is thought to pattern a distinct behavior.

Importantly, by definition, CPGs do not need phasic input, either descending or sensory, to generate their rhythm (Marder and Bucher, 2001). Thus, when deafferented, the neurons that comprise a CPG are capable of generating a "fictive" rhythm. However, that is not to say that the CPG works alone to pattern a behavior in an intact animal. Often, the CPG needs to be coordinated with other information, via sensory or cortical input, or neuromodulation from other brain areas, to pattern the full behavior (Grillner and El Manira, 2020). Furthermore, the neuronal mechanisms underlying the rhythmogenesis of each CPG may be distinct.

While hypothesized to exist for nearly all rhythmic motor behaviors, only few vertebrae CPGs have definitively been identified and characterized. A well-characterized CPG, and my area of study, is the respiratory central pattern generator in the ventral medulla of the brainstem.

THE RESPIRATORY CENTRAL PATTERN GENERATOR

Respiration is one of the most fundamental physiological processes that keeps us alive, oxygenating the blood pumped by the heart. An average person takes between 500 million - 1 billion breaths in a lifetime. Thus, the respiratory rhythm is necessarily robust and modulable. At its very core, basal respiration is thought to consist of an active inspiration, followed by a passive expiration, and the origin of this inspiratory rhythm is the preBötzinger complex (preBötC) in the hindbrain (Feldman et al., 2012; Del Negro et al., 2018).

First identified using serial transections of the brainstem until the point which breathing ceases, the preBötC lies in the ventral medulla, in an area ventral to the nucleus ambiguus (Smith et al., 1991). Lesion or inactivation of the preBötC leads to a cessation of respiration while stimulation of the preBötC increases breathing frequency and amplitude (Cui et al., 2016; Gray et al., 2001; Hayes et al., 2012; Tan et al., 2008). Neuronal activity in the preBötC correlates with phrenic nerve activity and inspiration in intact animals, suggesting its role as predominantly inspiratory, rather than expiratory. As expected for a CPG, a thin coronal section of the brainstem that contains the preBötC retains rhythmic activity, akin to a “fictive” respiratory rhythm. This activity can be measured, directly as rhythmic activity in the preBötC itself, or indirectly via recording from the hypoglossal nerve (CNXII) that is retained in the slice (Ruangkittisakul et al., 2014). A modified version of this slice preparation provided the basis for our *ex vivo* physiology experiments in Chapter 2. All these together suggest that the preBötzinger complex is the central pattern generator for breathing.

Given the wide range of physiological needs and behaviors of an animal, the respiratory rhythm needs to be highly adaptable to a variety of scenarios. This ranges from reflexive apneas to avoid inhalation of toxic gases or liquids, to adaptive adjustments in response to changes in blood gases, to coordination with certain orofacial behaviors. The preBötC can change in frequency or amplitude, bidirectionally, via interactions with many different brain areas. Breathing is modulated by sensory feedback, including lunch stretch and blood gases (O_2 via carotid body), in part via the nucleus tractus solitarus (NTS) (Song et al., 2011). The preBötC is also interconnected with other respiratory modulated structures in the brainstem such as the retrotrapezoid nucleus/parafacial respiratory group (RTN/pFRG), a chemosensory (CO_2-sensing) area that is also involved in the generation of active expiration (Mulkey et al., 2004; Onimaru and Homma, 2003). The patterning of an entire breath also involves input from the Kölliker-Fuse nucleus (KF), the parabrachial nucleus (PBN) and the putative Post inspiration Complex (PiCo) (Anderson et al., 2016; Dutschmann and Dick, 2012; Feldman et al., 2012; Song et al., 2011). Unsurprisingly, retrograde transsynaptic rabies tracing from the preBötC suggests many additional inputs may play a role in modulating the respiratory rhythm (Yang et al., 2020).

Despite its discovery more than 30 years ago, the precise mechanism of rhythm generation within the preBötC remains poorly defined. The leading model revolves around recurrent synaptic interactions between random "rhythmogenic" excitatory neurons in the preBötC (Kam et al., 2013; Del Negro et al., 2018). These excitatory "percolations" gradually increase in amplitude and synchrony during the passive expiratory period (Ashhad and Feldman, 2020). Upon reaching some threshold, these neurons recruit pattern generating neurons in the area to generate a full "burst", which subsequently drives premotor neurons and inspiratory muscles to produce an inspiration.

Alternative models suggest involvement of endogenously bursting "pacemaker" neurons which drive the respiratory rhythm in a manner similar to the rhythm in the heart (Peña et al., 2004). Regardless of the rhythmogenic mechanism, the duration of inspiration is limited by sensory feedback from lung stretch receptors via the vagus nerve and the NTS (Nonomura et al., 2017). Together, these form the neural basis of the basal (eupneic) respiration. During behaviors such as exercise where there is a change in blood gas composition, the conditional RTN/pFRG oscillator gets recruited and couples to the preBötC to produce an additional active expiration (Guyenet and Bayliss, 2015; Huckstepp et al., 2015).

OROFACIAL BEHAVIORS ARE COUPLED TO THE RESPIRATORY RHYTHM

In addition to eupneic and active breathing, breathing needs to be coordinated with a wide range of other vital behaviors, to avoid fatal blockage of the airway or to encourage active sensing of the environment. These include behaviors such as swallowing, licking, chewing, vocalization and whisking (Kleinfeld et al., 2014; Moore et al., 2014). Many of these are also rhythmic behaviors that are driven by underlying oscillators or central pattern generators. While the neuronal origins of most of these orofacial CPGs are unknown, they are thought to reside in the brainstem and coordinate with the preBötC for effective behavior.

Perhaps the most thoroughly characterized orofacial behavior is whisking. Through careful analysis of whisker movement and respiration, it was found that whisking is entirely entrained to breathing during sniffing, but absent in many other breathing contexts (Moore et al., 2013). Moreover, oscillatory whisking can continue during periods of induced apneas. This suggests that while whisking and breathing are typically coupled during periods of sniffing, perhaps for an

enhanced sensory role, they are separable oscillators that can also work independently of one another. Through rabies tracing, *in vivo* recordings, gain of function and loss of function experiments, it was found that an area termed the VIRT (ventral intermediate reticular tract) likely forms the CPG for whisking (Deschênes et al., 2016; Moore et al., 2013; Takatoh et al., 2013). Interestingly, breathing is thought to be able to reset the whisking pattern, thus putting it higher on the hierarchy of these coupled oscillators.

VOCALIZATIONS

One of the most fundamental and complex behaviors that is coordinated with breathing is vocalization (Nieder and Mooney, 2020a). Vocalization evolved as a distant form of communication between members of the same species and is often essential for survival of both the individual and the group. Various forms and modes of vocalization have been found in species as distant as fish and amphibians (Chagnaud et al., 2011).

Throughout evolution, vocalizations increased in organization and complexity, evolving into intricately structured forms of communication such as songs in birds and speech in humans (Petkov and Jarvis, 2012). Even within the same species, vocalizations vary depending on context and development. They can range from innate calls and cries to more complex songs and languages that convey complex semantic and emotional meaning.

Mouse USVs

While significantly less complex than human speech, rodent vocalization has been used as a model system to study key aspects of vocal communication. Mice vocalization occurs bimodally, first as

innate cries in neonates and later as exclusively social vocalizations in adults (Grimsley et al., 2011). Their vocalizations are ultrasonic, in the range of 20-100kHz (Ehret, 2018). The acoustic structure of adult mouse USVs have been well-characterized and described in detail (Castellucci et al., 2018; Holy and Guo, 2005; Vogel et al., 2019); however, it was only recently demonstrated that they correlate with specific social actions (Sangiamo et al., 2020). Adult vocalizations are thought to occur specifically in social contexts. Male mice will vocalize in response to nearby female mice, thus suggesting a potential role of adult vocalizations in mating (Ehret, 2018). Adult male mice also may vocalize when exposed to the urine of female mice in some contexts (Chabout et al., 2017).

Neonatal mouse vocalizations

Similar to humans and other mammals, neonatal rodents also produce vocalizations soon after birth (Caruso et al., 2018; Shair, 2018). These cries are induced when the pups are separated from their mom. While the precise physiological drive for these cries continues to be debated, their general role is thought to be a form of distressed communication, aimed at retrieval by their mom. This is particularly important as the pups are born blind and deaf, and lack locomotor activity, thus unable to return to the nest by themselves (Shair, 2018). Furthermore, young mouse pups are essentially poikilothermic, unable to regulate their own temperature, thus actively need their mom for maintaining their physiological body temperature (Caruso et al., 2018). Their cries, therefore, are absolutely critical for their early survival.

Similar to the USVs of adult mice, pup cries are also ultrasonic and occur in the 30-90kHz range, but the repertoire of calls are more limited in structure (Caruso et al., 2018). Neonatal mice

vocalizations occur in bouts and gradually decrease in number starting a week after birth until they stop occurring around twelve days after birth, concurrent with the pups' newfound visual, audio and locomotor development (Peleh et al., 2019). Note, neonatal mice also produce limited audible cries in response to painful stimuli, which are distinct from the USV cries.

Biomechanical mechanisms of mouse vocalization

Recent efforts have attempted to examine the biomechanical basis of mouse vocalization. Unlike vocalization in humans and other primates, where sound originates from vibration of the laryngeal vocal folds, mouse ultrasonic vocalizations are thought to be produced instead via a whistle-like mechanism (Kelm-Nelson et al., 2018; Riede, 2018; Riede et al., 2017). The ultrasonic sound is produced when expired air is forced through a tightly controlled laryngeal fold onto supraglottal structures such as the ventral pouch (Riede, 2018). Critical for this mechanism are the buildup of subglottal pressure by constriction of the upper airway and the activity of the larynx itself (Riede, 2011, 2018).

The larynx is thought to be a critical component of sound production in rodents as their activity is tightly correlated with duration and spectral features of the USVs. Furthermore, transection of the superior laryngeal nerve (which innervates the cricothyroid muscle of the larynx) or the recurrent laryngeal nerve (which innervates the other intrinsic laryngeal muscles), alter the number and quality or even completely eliminate USVs (Nunez et al., 1985; Wetzel et al., 1980). Unsurprisingly, the larynx does not work alone in sound production. The timing of laryngeal adduction must be coordinated with respiratory activity and other muscles in the upper airway for

proper sound production (Laplagne, 2018). The neural mechanism underlying laryngeal control and its coordination with respiration is unknown.

Neural circuits underlying vocalizations

The various muscles involved in vocalization are driven by laryngeal, respiratory and articular motor neuron pools in various parts of the brainstem and spinal cord. How these motor neurons are coordinated remains an open question. Given the seeming lack of direct anatomical connection between these various pools, one or more premotor groups of neurons likely coordinate their activity (Jürgens, 2009; Nieder and Mooney, 2020b). Anatomical and electrophysiological studies in squirrel monkeys suggest this likely lies in the reticular formation of the lower brainstem, where there are neurons with activity correlated with vocalization (Jürgens, 2009). One such putative area is the retroambiguus (RAm) where vocalization-correlated activity was found (Jürgens and Hage, 2007). However, the specific role of the RAm in vocalization remains unclear. Since vocalization occurs during the post-inspiratory part of expiration, brainstem areas involved in generating post-inspiratory activity (hypothesized to be the PiCo or KF), may also contribute. Whether one or more of these or other medullary structures are involved is unclear. Furthermore, how a vocalization pattern generator coordinates with the respiratory rhythm is also unknown. Understanding the circuits and pattern generator underlying vocalizations and its coordination with breathing will be the focus of Chapter 2.

In addition to medullary patterning center(s), endogenous vocalization also depends on a crucial structure known as the Periaqueductal Gray (PAG) in the midbrain. Stimulation of the PAG is sufficient to induce vocalizations, and lesion of the area or transection of the brainstem at this level

causes mutism in animals and humans (Esposito et al., 1999; Jürgens, 1994). However, given that perturbation of this area changes global amplitude of sound rather than specific spectral or rhythm features of the vocalizations, the PAG is thought to gate vocalization rather than directly patterning it (Gruber-Dujardin, 2010). Recently, a functional subset of neurons in the PAG was found to do exactly that - gating mouse USVs (Tschida et al., 2019). Upstream of the PAG, an inhibitory population of lateral preoptic neurons in the hypothalamus was found to trigger vocalizations by relieving a local inhibition of the PAG, potentially implicating it in emotional drive of vocalizations (Chen et al., 2021; Michael et al., 2020). Additionally, the NTS was also suggested to be necessary for vocalizations, specifically in neonates, potentially via a connection to expiratory neurons (Hernandez-Miranda et al., 2017).

Human speech deficits and clinical implications

Human speech disorders and deficits are most common during childhood development and include aphasia, mutism, stuttering, verbal dyspraxia, apraxia and autism (Kent, 2000). A prominent example is developmental apraxia of speech which involves a failed coordination of vocal motor patterning, in some cases caused by mutations in the Foxp2 gene (den Hoed and Fisher, 2020; Lai et al., 2001). On the other end of the age spectrum, speech deficit is often also present in neurodegenerative diseases such as amyotrophic lateral sclerosis and Parkinson's Disease (Dashtipour et al., 2018; Strong et al., 2008). A more complete understanding of the neural circuits underlying vocalizations may help us gain insights into the neurological underpinnings of these deficits, as well as develop novel therapy to treat these disorders. More broadly, control of vocalization and speech is control of the upper airway. A more profound understanding of the

regulation of the upper airway and its coordination with breathing may lead to alternative approaches to prevent common clinical conditions such as dysphagia and fatal aspirations.

REFERENCES

Anderson, T.M., Garcia, A.J., Baertsch, N.A., Pollak, J., Bloom, J.C., and Wei, A.D. (2016). A novel excitatory network for the control of breathing. Nature *536*, 76–80.

Ashhad, S., and Feldman, J.L. (2020). Emergent Elements of Inspiratory Rhythmogenesis: Network Synchronization and Synchrony Propagation. Neuron *106*, 482-497.e4.

Caruso, A., Sabbioni, M., Scattoni, M.L., and Branchi, I. (2018). Quantitative and Qualitative Features of Neonatal Vocalizations in Mice. In Handbook of Behavioral Neuroscience, p.

Castellucci, G.A., Calbick, D., and McCormick, D. (2018). The temporal organization of mouse ultrasonic vocalizations.

Chabout, J., Jones-Macopson, J., and Jarvis, E.D. (2017). Eliciting and Analyzing Male Mouse Ultrasonic Vocalization (USV) Songs. JoVE (Journal Vis. Exp. *2017*, e54137.

Chagnaud, B.P., Baker, R., and Bass, A.H. (2011). Vocalization frequency and duration are coded in separate hindbrain nuclei. Nat. Commun.

Chen, J., Markowitz, J.E., Lilascharoen, V., Taylor, S., Sheurpukdi, P., Keller, J.A., Jensen, J.R., Lim, B.K., Datta, S.R., and Stowers, L. (2021). Flexible scaling and persistence of social vocal communication. Nature *593*, 108–113.

Cui, Y., Kam, K., Sherman, D., Janczewski, W.A., Zheng, Y., and Feldman, J.L. (2016). Defining preBötzinger Complex Rhythm- and Pattern-Generating Neural Microcircuits In Vivo. Neuron *91*, 602–614.

Dashtipour, K., Tafreshi, A., Lee, J., and Crawley, B. (2018). Speech disorders in Parkinson's disease: pathophysiology, medical management and surgical approaches. Neurodegener. Dis. Manag. *8*, 337–348.

Deschênes, M., Takatoh, J., Kurnikova, A., Moore, J.D., Demers, M., Elbaz, M., Furuta, T., Wang, F., and Kleinfeld, D. (2016). Inhibition, Not Excitation, Drives Rhythmic Whisking. Neuron *90*, 374–387.

Dutschmann, M., and Dick, T.E. (2012). Pontine mechanisms of respiratory control. Compr. Physiol. *2*, 2443–2469.

Ehret, G. (2018). Characteristics of Vocalization in Adult Mice. Handb. Behav. Neurosci. *25*, 187–195.

Esposito, A., Demeurisse, G., Alberti, B., and Fabbro, F. (1999). Complete mutism after midbrain periaqueductal gray lesion. Neuroreport *10*, 681–685.

Feldman, J.L., Del Negro, C. a., and Gray, P.A. (2012). Understanding the Rhythm of Breathing: So Near, Yet So Far. Annu. Rev. Physiol. *75*, 121102144047002.

Gray, P.A., Janczewski, W.A., Mellen, N., McCrimmon, D.R., and Feldman, J.L. (2001). Normal breathing requires preBötzinger complex neurokinin-1 receptor-expressing neurons. Nat. Neurosci. *4*, 927–930.

Grillner, S., and El Manira, A. (2020). Current Principles of Motor Control, with Special Reference to Vertebrate Locomotion. Physiol. Rev. *100*, 271–320.

Grimsley, J.M.S., Monaghan, J.J.M., and Wenstrup, J.J. (2011). Development of Social Vocalizations in Mice. PLoS One *6*, e17460.

Gruber-Dujardin, E. (2010). Role of the periaqueductal gray in expressing vocalization. Handb. Behav. Neurosci. *19*, 313–327.

Guyenet, P.G., and Bayliss, D.A. (2015). Neural Control of Breathing and CO2 Homeostasis. Neuron *87*, 946–961.

Hayes, J. a, Wang, X., and Del Negro, C. a (2012). Cumulative lesioning of respiratory interneurons disrupts and precludes motor rhythms in vitro. Proc. Natl. Acad. Sci. U. S. A. *109*, 8286–8291.

Hernandez-Miranda, L.R., Ruffault, P.L., Bouvier, J.C., Murray, A.J., Morin-Surun, M.P., Zampieri, N., Cholewa-Waclaw, J.B., Ey, E., Brunet, J.F., Champagnat, J., et al. (2017). Genetic identification of a hindbrain nucleus essential for innate vocalization. Proc. Natl. Acad. Sci. U. S. A. *114*, 8095–8100.

den Hoed, J., and Fisher, S.E. (2020). Genetic pathways involved in human speech disorders. Curr. Opin. Genet. Dev. *65*, 103–111.

Holy, T.E., and Guo, Z. (2005). Ultrasonic songs of male mice. PLoS Biol. *3*, 1–10.

Huckstepp, R.T.R., Cardoza, K.P., Henderson, L.E., and Feldman, J.L. (2015). Role of Parafacial Nuclei in Control of Breathing in Adult Rats. J. Neurosci. *35*, 1052–1067.

Jürgens, U. (1994). The role of the periaqueductal grey in vocal behaviour. Behav. Brain Res. *62*, 107–117.

Jürgens, U. (2009). The Neural Control of Vocalization in Mammals: A Review. J. Voice *23*, 1–10.

Jürgens, U., and Hage, S.R. (2007). On the role of the reticular formation in vocal pattern generation. Behav. Brain Res. *182*, 308–314.

Kam, K., Worrell, J.W., Janczewski, W.A., Cui, Y., and Feldman, J.L. (2013). Distinct Inspiratory Rhythm and Pattern Generating Mechanisms in the preBotzinger Complex. J. Neurosci. *33*, 9235–9245.

Kelm-Nelson, C.A., Lenell, C., Johnson, A.M., and Ciucci, M.R. (2018). Laryngeal Activity for

Production of Ultrasonic Vocalizations in Rats. Handb. Behav. Neurosci. *25*, 37–43.

Kent, R.D. (2000). Research on speech motor control and its disorders: a review and prospective. J. Commun. Disord. *33*, 391–428.

Kleinfeld, D., Deschênes, M., Wang, F., and Moore, J.D. (2014). More than a rhythm of life: Breathing as a binder of orofacial sensation. Nat. Neurosci. *17*, 647–651.

Lai, C.S.L., Fisher, S.E., Hurst, J.A., Vargha-Khadem, F., and Monaco, A.P. (2001). A forkhead-domain gene is mutated in a severe speech and language disorder. Nature *413*, 519–523.

Laplagne, D.A. (2018). Interplay Between Mammalian Ultrasonic Vocalizations and Respiration. Handb. Behav. Neurosci. *25*, 61–70.

Marder, E., and Bucher, D. (2001). Central pattern generators and the control of rhythmic movements. Curr. Biol.

Michael, V., Goffinet, J., Pearson, J., Wang, F., Tschida, K., and Mooney, R. (2020). Circuit and synaptic organization of forebrain-to-midbrain pathways that promote and suppress vocalization. Elife *9*, 1–29.

Moore, J.D., Deschênes, M., Furuta, T., Huber, D., Smear, M.C., Demers, M., and Kleinfeld, D. (2013). Hierarchy of orofacial rhythms revealed through whisking and breathing. Nature.

Moore, J.D., Kleinfeld, D., and Wang, F. (2014). How the brainstem controls orofacial behaviors comprised of rhythmic actions. Trends Neurosci. *37*, 370–380.

Mulkey, D.K., Stornetta, R.L., Weston, M.C., Simmons, J.R., Parker, A., Bayliss, D.A., and Guyenet, P.G. (2004). Respiratory control by ventral surface chemoreceptor neurons in rats. Nat. Neurosci. 2004 712 *7*, 1360–1369.

Del Negro, C.A., Funk, G.D., and Feldman, J.L. (2018). Breathing matters. Nat. Rev. Neurosci.

19, 351–367.

Nieder, A., and Mooney, R. (2020a). The neurobiology of innate, volitional and learned vocalizations in mammals and birds. Philos. Trans. R. Soc. B *375*.

Nieder, A., and Mooney, R. (2020b). The neurobiology of innate, volitional and learned vocalizations in mammals and birds. Philos. Trans. R. Soc. B Biol. Sci. *375*.

Nonomura, K., Woo, S.H., Chang, R.B., Gillich, A., Qiu, Z., Francisco, A.G., Ranade, S.S., Liberles, S.D., and Patapoutian, A. (2017). Piezo2 senses airway stretch and mediates lung inflation-induced apnoea. Nature *541*, 176.

Nunez, A.A., Pomerantz, S.M., Bean, N.J., and Youngstrom, T.G. (1985). Effects of laryngeal denervation on ultrasound production and male sexual behavior in rodents. Physiol. Behav.

Onimaru, H., and Homma, I. (2003). A novel functional neuron group for respiratory rhythm generation in the ventral medulla. J. Neurosci. *23*, 1478–1486.

Peleh, T., Eltokhi, A., and Pitzer, C. (2019). Longitudinal analysis of ultrasonic vocalizations in mice from infancy to adolescence: Insights into the vocal repertoire of three wild-type strains in two different social contexts. PLoS One *14*.

Peña, F., Parkis, M.A., Tryba, A.K., and Ramirez, J.M. (2004). Differential contribution of pacemaker properties to the generation of respiratory rhythms during normoxia and hypoxia. Neuron *43*, 105–117.

Petkov, C.I., and Jarvis, E.D. (2012). Birds, primates, and spoken language origins: Behavioral phenotypes and neurobiological substrates. Front. Evol. Neurosci. *4*, 12.

Riede, T. (2011). Subglottal pressure, tracheal airflow, and intrinsic laryngeal muscle activity

during rat ultrasound vocalization. J. Neurophysiol. *106*, 2580–2592.

Riede, T. (2018). Peripheral Vocal Motor Dynamics and Combinatory Call Complexity of Ultrasonic Vocal Production in Rats. In Handbook of Behavioral Neuroscience, p.

Riede, T., Borgard, H.L., and Pasch, B. (2017). Laryngeal airway reconstruction indicates that rodent ultrasonic vocalizations are produced by an edge-tone mechanism. R. Soc. Open Sci. *4*.

Ruangkittisakul, A., Kottick, A., Picardo, M.C.D., Ballanyi, K., and Del Negro, C.A. (2014). Identification of the pre-Bötzinger complex inspiratory center in calibrated "sandwich" slices from newborn mice with fluorescent Dbx1 interneurons. Physiol. Rep.

Sangiamo, D.T., Warren, M.R., and Neunuebel, J.P. (2020). Ultrasonic signals associated with different types of social behavior of mice. Nat. Neurosci. 2020 233 *23*, 411–422.

Shair, H.N. (2018). Infantile Vocalizations in Rats. Handb. Behav. Neurosci. *25*, 129–137.

Smith, J.C., Ellenberger, H.H., Ballanyi, K., Richter, D.W.D.W., Feldman, J.L., Smrih, J.C., Ellenberger, H.H., Ballanyi, K., Formaker, B.K., Hill, D.L., et al. (1991). Pre-Botzinger complex: a brainstem region that may generate respiratory rhythm in mammals. Science (80-.). *254*, 726–729.

Song, G., Xu, H., Wang, H., MacDonald, S.M., and Poon, C.S. (2011). Hypoxia-excited neurons in NTS send axonal projections to Kölliker-Fuse/parabrachial complex in dorsolateral pons. Neuroscience *175*, 145–153.

Strong, M.J., Grace, G.M., Orange, J.B., and Leeper, H.A. (2008). Cognition, Language, and Speech in Amyotrophic Lateral Sclerosis: A Review. Http://Dx.Doi.Org/10.1080/01688639608408283 *18*, 291–303.

Takatoh, J., Nelson, A., Zhou, X., Bolton, M.M.L., Ehlers, M.D., Arenkiel, B.R., Mooney, R., and Wang, F. (2013). New Modules Are Added to Vibrissal Premotor Circuitry with the Emergence of Exploratory Whisking. Neuron *77*, 346–360.

Tan, W., Janczewski, W.A., Yang, P., Shao, X.M., Callaway, E.M., and Feldman, J.L. (2008). Silencing preBötzinger Complex somatostatin-expressing neurons induces persistent apnea in awake rat. Nat. Neurosci. *11*, 538–540.

Tschida, K., Michael, V., Takatoh, J., Han, B.X., Zhao, S., Sakurai, K., Mooney, R., and Wang, F. (2019). A Specialized Neural Circuit Gates Social Vocalizations in the Mouse. Neuron *103*, 459-472.e4.

Vogel, A.P., Tsanas, A., and Scattoni, M.L. (2019). Quantifying ultrasonic mouse vocalizations using acoustic analysis in a supervised statistical machine learning framework. Sci. Reports 2019 91 *9*, 1–10.

Wetzel, D.M., Kelley, D.B., and Campbell, B.A. (1980). Central control of ultrasonic vocalizations in neonatal rats: I. Brain stem motor nuclei. J. Comp. Physiol. Psychol. *94*, 596–605.

Yang, C.F., Kim, E.J., Callaway, E.M., and Feldman, J.L. (2020). Monosynaptic Projections to Excitatory and Inhibitory preBötzinger Complex Neurons . Front. Neuroanat. *14*, 58.

CHAPTER 2: A NOVEL RETICULAR OSCILLATOR IN THE BRAINSTEM SYNCHRONIZES NEONATAL CRYING WITH BREATHING

BACKGROUND

Rhythmicity underlies both human speech and animal vocalizations. For instance, speech oscillates in volume with each syllable (Poeppel and Assaneo, 2020), the communicative calls of marmosets are composed of repeating units (Pomberger et al., 2018), and the timing of songbird syllables are regularly spaced as they learn to sing (Okubo et al., 2015). These and other examples suggest that the tempo of sounds within vocalizations is innately encoded. Indeed, the rhythmic vocalizations of midshipman fish are timed by pacemaker neurons in the hindbrain (Chagnaud et al., 2011). It has therefore been hypothesized that the rhythmicity of mammalian sound production is created by hardwired neural circuits in the brainstem, but evidence to support this theory is lacking.

The innate vocalization motor program is initiated by brainstem projections from the midbrain periaqueductal gray (Tschida et al., 2019); however, the neural circuitry required to fully orchestrate these vocalizations remains poorly understood (Hage, 2009; Zhang and Ghazanfar, 2020). Moreover, because mammalian vocalizations are produced by the concerted activity of sound producing (laryngeal), articulating (tongue) and breathing (diaphragm and intercostal) muscles (Riede, 2018), they must be seamlessly integrated with the breathing rhythm. We hypothesized that the vocalization motor patterning system is anatomically and functionally connected to the neural circuit for breathing in the brainstem. We also predicted that this circuit encodes rhythmicity within vocalizations. Here, by studying the neural control of instinctive cries

produced by neonatal mice, which are analogous to the cries of human infants (Ehret, 2005; Long and Hull, 1961; Wilder, 1974), we elucidate the brainstem mechanism that patterns and paces mammalian vocalizations.

We found that neonatal cries contain one, two, three or more regularly spaced syllables within a single breath. The production of sound requires closure (adduction) of the larynx and each syllable is separated by reactivation of inspiratory breathing muscles. Thus, the standard vocalization motor program – inspiration followed by laryngeal adduction – must be repeatedly engaged within a single breath to generate multisyllabic cries. Our identification and characterization of the iRO, which produces a fast and autonomous rhythm nested within a slower breathing rhythm, provides a mechanism for such repetition. Each burst of iRO activity patterns the motor program to enable articulation of a single cry, and multiple iRO bursts within a breath generate multisyllabic cries. Ablation or pharmacological inhibition of the iRO either eliminates or modifies normal neonatal cry rhythms and disrupts multisyllabic cry production. And brief activation of the iRO neurons during an endogenous cry adds a syllable, while excitation during calm breathing initiates an ectopic cry bout.

METHODS

Experimental model and subject details

C57Bl/6J, *Snap25-GCaMP6s* (*Snap25*$^{tm3.1Hze}$) (Madisen et al., 2015), *Slc17a6*-Cre (Vong et al., 2011), *Gad2*-Cre (Taniguchi et al., 2011), *Slc32a1*-Cre (Vong et al., 2011), *Slc6a5*-Cre (Sherman et al., 2015), *RIKEN-Slc6a5*-Cre (Kakizaki et al., 2017), *Dbx1*-Cre (Bielle et al., 2005), *Foxp2*-Cre (Rousso et al., 2016), *Chat*-Cre (Rossi et al., 2011), *Egr2*-Cre (Voiculescu et al., 2000), *Neurod6*-Cre (Schwab et al., 2000), *Penk*-Cre (Tasic et al., 2018), *Parv*-Cre (Hippenmeyer et al., 2005), *Tac1*-Cre (Harris et al., 2014), *Npy*-Cre (Milstein et al., 2015), ROSA-LSL-G-TVA (Gt(ROSA)26Sor$^{tm1(CAG-RABVgp4,-TVA)Arenk}$) (Takatoh et al., 2013), ROSA-LSL-GCaMP6s (Ai96) (Madisen et al., 2015), ROSA-LSL-GCaMP6f (Ai95) (Madisen et al., 2015), ROSA-LSL-EYFP (Srinivas et al., 2001), *Slc17a6*-FlpO (Daigle et al., 2018), RC::FLTG (Plummer et al., 2015), and R26-LSL-FSF-ReaChR-mCitrine (Hooks et al., 2015) have been described. Mice were housed in a 12-hour light/dark cycle with unrestricted food and water. All animal experiments were performed in accordance with national and institutional guidelines with standard precautions to minimize animal stress and the number of animals used in each experiment.

Recombinant viruses

All viral procedures followed the Biosafety Guidelines approved by the University of California, San Francisco (UCSF) Institutional Animal Care and Use Program (IACUC) and Institutional Biosafety Committee (IBC). The following viruses were used: oG SiR G-Deleted Rabies-FlpO-mCherry, G-Deleted Rabies-eGFP, G-Deleted Rabies-mCherry (all >1.0x10^8 TU/mL, The Viral Vector Core at the Salk Institute for Biological Sciences or Janelia Viral Tools) and HSV-hEF1a-

Rabies G (RN700), HSV-hCMV-YTB (Gene Delivery Technology Core Massachusetts General Hospital).

Methods details

Plethysmography, vocalization, and analysis

Breathing pressure changes and vocalizations were measured in neonatal mice (P2-P4) in a custom prepared whole animal plethysmography chamber at room temperature (23°C, **Figure 2.1a**) and constant humidity. The top of the chamber is sealed by the microphone and enables the volume of the chamber to be appropriately adjusted to the size of the neonate. Pups were removed from their home cage and placed in the recording chamber for 2 x 5 minutes of recording and returned to their home cage. Mice were recorded for 1-2 more times throughout day, following the same protocol, to get a consistent baseline. Vocalization was recorded using an Avisoft Bioacoustics UltraSoundGate CM16/CMPA microphone and chamber pressure was transmitted to a spirometer (AD Instruments). The microphone and spirometer were connected to a PCI DAQ device (PCI NIDAQ 6251), allowing respiration and vocalization data to be simultaneously acquired at 400kHz using custom Matlab (MathWorks) code. Light tapping of the chamber with a metal rod show a constant <2ms difference in timing of changes in sound and pressure change.

The respiration and vocalization data were analyzed offline in Matlab. The pressure trace was downsampled, filtered, and breathing was segmented using the troughs and peaks of measured pressure as surrogates for onset of inspiration and expiration, along with quality control metrics. Pressure change was defined as the first derivative of the pressure trace with respect to time. Given differences in tidal volume due to the intrinsic variance of lung volumes of pups at these ages

(discussed further below), large breaths were defined as the minimal tidal volume that must be exceeded for 95% of cries in a trace. USVs were detected using code modified from the Holy Lab (Holy and Guo, 2005). The parameters used to detect vocalizations are: spectral purity threshold > 0.3, spectral discontinuity threshold < 0.8., cry duration threshold > 2ms, minimal inter-syllable interval > 15ms, and mean frequency threshold > 30kHz. Airflow peaks were determined using the findpeaks function (Matlab).

Since barometric whole-body plethysmography imprecisely measures airflow and tidal volume (Mortola and Frappell, 1998), tidal volume in neonates correlates with their weight instead of age (Lim et al., 2014), we have reported the breathing measurements as changes in pressure that are in arbitrary units. Thus, we have not compared the amplitude of breathing airflow between animals nor reported it as mLs/sec. However, these measurements still allow for the changes in breathing within the same animal to be directly compared as arbitrary units.

Genioglossus and intercostal EMG

Neonatal mice were briefly anaesthetized by hypothermia. Paired EMG electrodes made from Teflon-coated multistranded stainless steel wires (Cooner Wire) and small suture needles (Fine Science Tools) were passed through the genioglossus or intercostal muscles and secured with a knot (Pagliardini et al., 2011). Teflon was removed from a small (<0.5mm) segment of the wire adjacent to the knot, allowing the exposed wire to be embedded in the GG or intercostal muscles. The EMG electrodes were connected to an AC differential amplifier (A-M systems AM1800), band-pass filtered (300Hz/10kHz) and digitized with an PCI DAQ device (PCI NIDAQ 6251), along with USV and respiration measurements, allowing for synchronous data acquisition at

250kHz (single EMG) or 200kHz (dual EMGs). The EMG data was rectified and integrated offline with a modified Paynter filter in Matlab.

Laryngeal (TA) muscle lesion

Neonatal mice were anaesthetized by hypothermia and gently fixed in the supine position. A small 2mm incision was made ventrally in the neck, and the muscles overlying the thyroid cartilage were carefully isolated with sutures. A microincision was made on the thyroid cartilage with the sharp tip of a 28G needle, and a small bipolar electrode (Microprobes) was inserted into the TA muscle. The muscle was lesioned by passing a current of 500μA for 2.5-5 seconds. For the sham group, the same protocol was followed except no current was passed after inserting the bipolar electrodes into the TA muscle. The neck was sutured, and mouse was allowed to recover fully before recording of attempted vocalizations. After the recording, the larynx was fully dissected to confirm the site of the lesion.

Stereotaxic electrolytic lesion, injection and stimulation

Bilateral stereotaxic injections and electrolytic lesions were performed in neonatal mice anaesthetized by hypothermia. The mouse was oriented on a stereotaxic frame (Kopf) with a neonatal adaptor (Stoelting) such that bregma was 1.5mm below lambda. In this position, the coordinates used for the iRO node were: P2: 2.50 mm posterior, 3.35 mm ventral from surface of the brain, ± 0.82 mm lateral from lambda; P3: 2.30 mm posterior, 3.50 mm ventral from surface of the brain, ±0.87 mm lateral from lambda. Electrolytic lesions were performed with a concentric bipolar microelectrode (FHC) by passing a current of 30-80μA for 2-5 seconds. Animals were fully recovered on a heat pad and returned to their nest. After lesions, neonates recovered for at

least 24 hours before breathing and vocalizations were recorded again. After the post lesion recordings were performed, lesion sites were validated by both anatomical localization visualized by light microscopy and changes of GCaMP6s activity in the iRO and preBötC in a medullary slice preparation (described below). Lesions were classified as bilateral "off" target from the iRO node, bilateral "on" target, or unilateral "on" target. Criteria used to classify lesions as "on" target: 1) immediately medial to the cNA (within 50-100μm), 2) dorsal to the BötC, 3) did not contain the cNA, and 4) the absence of the iRO rhythm in synaptic blockers measured by changes in GCaMP6s fluorescence. "off" target lesions were used as the control group and therefore all breathing, vocalization, and physiology validation were performed as a blinded study. The same coordinates were used for stereotaxic injection. Approximately 70nL of nifedipine (10μM), 70nL of carbenoxolone (1mM), or 70nL of ACSF were injected with a Nanoject III (Drummond), at a rate of 2-3nLs/second. The animals were recovered on a heating pad. Breathing and vocalization were recorded ~30 minutes after injection. Injection sites were confirmed by histological analysis of co-injected dye. For stimulation studies, a tungsten microelectrode (MicroProbes) was stereotaxically lowered into the iRO area and rigidly implanted using superglue. The animals were recovered on a heating pad for 30 minutes. Stimulation current (10ms train of biphasic current pulses at 400Hz: 0.4 ms pulse, 2.1ms between each pulse) was delivered via an isolated pulse stimulator (AM Systems). The stimulation intensity was gradually increased from 50μA to 600μA or until a phenotype was observed. The location of the electrode was verified histologically following each experiment.

In vivo optogenetics

Neonatal mice were cryoanesthetized and positioned on the stereotaxic frame as described above. A single fiber optic ferrule and fiber (1.25mm ferrule, 200µm core fiber, Thorlabs) was lowered into the brain using the coordinates for the iRO node, positioned approximately 200µm above the iRO node. The ferrule was superglued in place on the skull, and the mice were allowed to recover on a heating pad for 30 minutes. Following recovery, the mouse was connected to a DPSS laser (532 nM, Shanghai Laser and Optics Co., ~20 mW) using patch cable (Doric lenses) and lowered into the chamber for recording. The laser was controlled by TTL Pulse Generator (Doric lenses). Single pulses were triggered near the peak of expiration using the PowerLab (ADInstruments) fast response output connected to the TTL. Train of pulses were triggered randomly. All data was analyzed with a custom Matlab code to align pulses with ultrasonic sound and breathing.

Laryngeal Rabies virus and Cholera toxin injections

Rabies tracing was performed using Chat-Cre;ROSA-LSL-G-TVA (Gt(ROSA)26Sor$^{tm1(CAG-RABVgp4,-TVA)Arenk}$) mice and the G-Deleted Rabies viruses listed above. For a subset of tracing experiments, a G-Deleted Rabies virus was coinjected with HSV hEF1a-Rabies G in C57Bl/6J or *Snap25*-Gcamp6s mice. Neonatal mice at P0 were cryoanesthetized and fixed in various positions with adhesive that were suitable for the muscle being injected. Each muscle was injected using a Nanoject III (Drummond). Between 30 to 150 nLs (depending on muscle) of virus were injected unilaterally, depending on the muscle, at a rate of 5-10nL/sec. Muscles injected were the cricothyroid, thyroarytenoid, genioglossus, masseter, whisker pad, and nose in order to trace the premotor neurons for vocalization (larynx, genioglossus), swallowing (genioglossus), chewing (masseter), and whisking (whiskers), and nose movement (nose). For injection into the laryngeal

muscles (thyroarytenoid and cricothyroid), the overlaying muscles were bluntly dissected and carefully isolated with sutures. A microincision was made on the thyroid cartilage with the sharp tip of a 28G needle to allow for insertion of the micropipette into the thyroarytenoid muscle. Normal saline was used to flush the overlying area to prevent any nonspecific infection and labeling. After injections, the neonates were recovered on a heat pad and then returned to their nest. Neonates recovered for 4 days and then were euthanized for medullary slice preparation (described below). Rabies traced fluorescent neurons were identified and their electrophysiological activity was recorded. Cholera Toxin Subunit B (C34776, Life Technologies) injections were performed as described above, except they were only into the thyroarytenoid and cricothyroid muscles, and animals recovered for 2 days before euthanasia for brainstem slice preparation. All injection solutions contained fast-green dye to confirm that only the correct muscle was injected.

Histology

4-7 days after injection of the viral cocktail, pups were transcardially perfused with 10mL of heparinized saline followed by 10mL of 4% PFA in phosphate-buffered saline (PBS). The brains were dissected and postfixed overnight in 4% PFA, cryoprotected in 15 or 30% sucrose PBS (w/v) and embedded in OCT. The embedded brains were cryosectioned at 20 or 30μm. Sections were then blocked for 1 hour in 0.5% triton-X PBS and 4% normal horse or goat serum and subsequently incubated with a solution of primary antibodies in the blocking solution at 4°C overnight. For samples that required the use of a mouse primary antibody, the sections were further blocked using the Mouse on Mouse Blocking Reagent (Vector Labs, MKB-2213-1) for 1 hour prior to incubation in the primary antibody. The primary antibodies used are: chicken anti-GFP (Aves, GFP-1020), goat anti-ChAT (Millipore, AB144p), rabbit anti-GFP (Invitrogen, A11122), rabbit anti-phox2b

(Jean-François Brunet lab), mouse anti-phox2b (Santa Cruz, B-11), rat anti-RFP (Chromotek, 5F8). The sections were washed in PBS, and the incubation procedure was then repeated with a solution containing secondary antibodies for 1-4 hours at 4°C. The secondary antibodies used are: donkey anti-chicken 488 (Jackson ImmunoResearch, 703-545-155), donkey anti-chicken Cy5 (Jackson ImmunoResearch, 703-176-155), donkey anti-goat Cy5 (Jackson ImmunoResearch, 705-606-147), donkey anti-rabbit 488 (Jackson ImmunoResearch, 711-545-152) donkey anti-rabbit Cy5 (Jackson ImmunoResearch, 712-165-153), donkey anti-rat Cy3 (Jackson ImmunoResearch, 711-495-152), goat anti-mouse Alexa Fluor 647 (Invitrogen, 21236). The slides were washed in PBS, air dried and mounted using mowiol or fluorescence mounting medium (Dako) and coverslipped. Epifluorescence and confocal images were acquired with a NanoZoomer S210 digital slide scanner (Hamamatsu Photonics), Leica SP5 confocal microscope (Leica), or Nikon CSU-W1 Spinning Disk (Nikon). For RearChR^{+}, only membrane-bound mCitrine were quantified.

Slice preparation and electrophysiology

550 to 650µm-thick transverse medullary slices which contain the preBötC and cranial nerve XII (XIIn) were prepared from neonatal P0-5 *Snap25*-GCaMP6s, *Chat-Cre;*ROSA-LSL-G-TVA (Gt(ROSA)26Sor$^{tm1(CAG-RABVgp4,-TVA)Arenk}$) rabies injected, HSV and rabies injected, and lesioned animals were prepared as described (Ruangkittisakul et al., 2014). Briefly, slices were cut in ACSF containing (in mM): 124 NaCl, 3 KCl, 1.5 $CaCl_2$, 1 $MgSO_4$, 25 $NaHCO_3$, 0.5 NaH_2PO_4, and 30 D-glucose, equilibrated with 95% O_2 and 5% CO_2 (4°C, pH=7.4). The rostral side of the slice was taken 100µm caudal to the end of the facial nucleus, at the rostral end of the compact nucleus ambiguus. All recordings were performed in the ACSF described above except the K^+ was raised to 9 mM, and osmotically balanced, and temperature was raised to 27.5-28.5°C. This elevation of

extracellular K^+ enables spontaneous preBötC activity to activate the hypoglossal motor nucleus (Kam et al., 2013). The iRO neurons were identified by either monosynaptic rabies virus tracing from the thyroarytenoid muscle or by the presence of the iRO rhythm in *Snap25*-GCaMP6s mice (expiratory oscillation or gap-junction-dependent oscillation). If the neurons were identified without the cocktail of fast synaptic blockers, after each experiment the antagonists were applied to ensure the neuron contained the iRO signature rhythm (gap-junction-dependent oscillation). The preBötC neural activity was inferred by the activity recorded from either XIIn rootlet or as population activity directly from the XII motor nucleus using suction electrodes, amplified and low/high pass filtered at 3kHz/400Hz, rectified, integrated and digitized using Digidata 1550B. Current and voltage clamp recordings of single neurons were performed with a MultiClamp700A or B using pClamp9 and digitized at 10000 Hz. Internal consisted of K^+-Gluconate (135mM), EGTA (1.1mM), NaCl (5mM), $CaCl_2$ (0.1mM), HEPES (10mM), ATP (2mM), GTP (0.3mM). Alexa-488 was used to fill recorded neurons. For experiments in synaptic blockers, NBQX (10µM, Abcam, ab120046) or CNQX (10µM, Abcam, ab120044), D-APV (50µM, Alomone Labs, D-145), picrotoxin (100µM, Abcam, ab120315), strychnine (1µM, Sigma Aldrich, S0532) were bath applied after an initial 20-minute recovery period in 9mM K^+ ACSF. For pharmacological analysis of rhythmic activity, the following peptides and drugs were bath applied: Carbenoxolone (50-150µM, Sigma-Aldrich), 18ß-glycyrrhetinic acid (150µM, Sigma-Aldrich, G10105), Meclofenamic acid (100µM. Fisher Scientific, AAJ6048403), tetrodotoxin (TTX, 1µM, Abcam, ab120054), Substance P (200nM, Abcam, ab120170), DAMGO (20-200nM, Abcam, ab120674), Nifedipine (2µM, Tocris, 1075), Bay K8644 (100nM, Tocris, 154410), Veratridine (250nM, Abcam, ab120279), ZD7288 (100µM, Abcam, ab120102), Riluzole (20µM, Abcam, ab120272), Mibefradil (10µM, Tocris, 219810), Iberiotoxin (50nM, Alomone Labs, STI-400), UCL1684

(50nM, Tocris, 13105). For pharmacological analysis of rhythmic activity, the drugs were added to the internal recording solution: QX314 chloride (5mM, Tocris, 2313). For optogenetic studies, fluorescently tagged, membrane bound ReaChR-mCitrine neurons were recorded, and an LED (Excelitas) source was used to illuminate the neurons.

Gap junction electrical coupling

Gap junctions between the iRO neurons were validated by both electrical coupling. To determine if neurons were electrically coupled, the iRO neurons were identified by Snap25-GCaMP6s activity in 9mM K^+ ACSF containing synaptic blockers. After a pair of iRO neurons were patched, TTX was bath applied to silence the spontaneous rhythm. A current step of 500pA was applied to one neuron and a corresponding change in membrane potential was recorded. After, a similar current protocol was applied to the alternative neuron.

Quantification and statistical analysis

Statistics

Statistical tests were performed on data collected from electrolytic lesions, electrical stimulation, nifedipine, ACSF, and carbenoxolone stereotaxic injection, and optogenetic stimulation. For all datasets, a Shapiro-Wilks test was first performed to assess normality of the distribution. P-value <0.05. If both groups to be compared had normal distributions, a one tailed t-test with unequal variance was performed. If one or both datasets were not normal, then a Wilcox Rank Sum was performed. For electrolytic lesions, the t-test compared "off" target to bilateral "on" target lesions and “off” target to unilateral lesions. For pharmacology microinjections, ACSF was compared with nifedipine and carbenoxolone.

RESULTS

Neonatal cries comprise syllables that are rhythmically timed within a breath.

To study the coordination of vocalizations with breathing, we induced instinctive ultrasonic vocalizations (USVs) by removing neonatal mice from their nests. These cries were recorded while breathing was monitored by unrestrained barometric plethysmography (Hernandez-Miranda et al., 2017) (**Figure 2.1A**). Cries were characterized by increased inspiratory and expiratory airflow coupled with USVs in the 50-150 kHz range and occurred in bouts of 9.7 ± 0.6 breaths (average ± SEM, n = 16 pups) (**Figures 2.1A-C**). Most cry breaths comprised one distinct vocalization, or syllable, that commenced ~10-20 milliseconds after the onset of expiration and coincided with peak expiratory airflow (**Figures 2.1D, F-G**). However, cry breaths in the middle of a bout tended to include two, three, or sometimes more elements, and were therefore designated as multisyllabic (**Figures 2.1C-D**). In these cases, the onset of each syllable was timed to follow rhythmic local peaks in expiratory airflow, and the syllables were separated by a period of silence associated with a dip in airflow (**Figures 2.1D, F-G**). Syllables within unisyllabic cries were longer than those in multisyllabic cries, and syllables progressively increased in length during multisyllabic cries (**Figure 2.1E**). The rhythmicity of postnatal mouse cries led us to hypothesize that they were timed by a fast conditional oscillator nested within a slower breathing pattern.

Cry syllables are coordinated with the respiratory motor program.

Murine adult vocalizations are produced when airflow through a closed (adducted) glottis becomes rapid and then turbulent after colliding with the laryngeal cartilage (Johnson et al., 2010; Mahrt et al., 2016). To explore whether neonatal cries similarly require laryngeal adduction, we disrupted the thyroarytenoid (TA) muscle, one of the key muscles that closes the larynx. Bilateral electrolytic

lesion of the TA eliminated the characteristic spectrogram features of cries despite the retention of augmented airflow, rate, and regularity during cry bouts (**Figures 2.2A, 2.9**). Surprisingly, attempted cry breaths after TA lesion still showed airflow oscillations reminiscent of multisyllabic cries (**Figure 2.2B**). This suggested that, although laryngeal adduction is required for producing the sound of each cry syllable, the airflow dip that separates the syllables is generated by a distinct mechanism.

Because the larynx adducts immediately after inspiration during basal breathing (Del Negro et al., 2018), we wondered if the airflow dips that preceded laryngeal adductions during cry syllables are also patterned by an inspiratory motor program. In this way, inspiration would be ectopically initiated during expiration. Indeed, signatures of the inspiratory motor program, such as genioglossus (tongue) and intercostal muscle activity (Huckstepp et al., 2016), preceded each cry syllable during airflow dips (**Figures 2.2C-D**). Inspiratory muscle activity was maximal approximately halfway between two expiratory airflow peaks (**Figure 2.2E**), during which time, body wall movements mimicked inspiration (**Figure 2.10**). These data suggest that the proposed oscillator can time multisyllable cries by cyclically re-engaging the respiratory motor program to generate inspiration followed by laryngeal adduction within a slower breath (**Figure 2.2F**).

The medullary brainstem contains a cluster of premotor neurons for sound production and articulation.

To begin investigating the underlying circuit driving rhythmic cries, we first sought to identify premotor neurons to the key muscles that produce sound, including the TA and cricothyroid (CT) muscles that adduct the larynx. We thus performed monosynaptic viral tracing from TA and CT

motor neurons, using two methods: 1) microinjecting TA or CT muscles with glycoprotein-deleted rabies virus (ΔG-rabies-mCherry), complemented with glycoprotein-expressing herpes simplex virus (HSV-G) in wildtype neonates or 2) microinjecting these muscles with ΔG-rabies-mCherry in mice expressing the glycoprotein in all motor neurons (ChAT-Cre;ROSA-LSL-G-TVA) (**Figure 2.3A**). We confirmed that laryngeal muscle injections were restricted to the intended muscle (**Figure 2.3A**). Four to seven days after injection, we found infected neurons arising from both muscles in similar areas throughout the ventral respiratory column (TA, n = 10; CT, n = 10) (**Figure 2.11**). Traced premotor neurons were distinguished from motor neurons by the absence of Phox2b transcription factor expression (Pattyn et al., 2000) and were found medial to the compact nucleus ambiguus (cNA) in the rostral ventral intermediate reticular formation (rv-iRF), the Bötzinger complex (BötC), the preBötzinger complex (preBötC), and the retroambiguus (RAm) (**Figures 2.3A-C** and **2.11**). To characterize the neurotransmitter used by these various TA premotor neuron pools, we injected ΔG-mCherry-rabies and HSV-G into the TA muscle of transgenic neonatal mice expressing labeled glutamatergic (Vglut2-Cre;ROSA-LSL-YFP) or GABAergic (Vgat-Cre;ROSA-LSL-YFP) neurons. TA premotor neurons within the rv-iRF were *Vglut2*-positive, those in other respiratory brainstem centers including the BötC and RAm were mostly *Vgat*-positive, and those in the preBötC were either *Vglut2*-positive or *Vgat*-positive (**Figures 2.3C-D**).

We next asked whether premotor neurons for muscles of articulation, such as the tongue, overlap with one or more laryngeal premotor neuron clusters. To directly compare the spatial distribution of TA and tongue premotor neurons, we microinjected the tongue and TA with ΔG-rabies-expressing GFP or mCherry, respectively. Tongue premotor neurons primarily localized to the iRT

(**Figure 2.3E**, as in Stanek et al. 2014). Therefore, of the areas that contained TA premotor neurons, only the rv-iRF contained neurons premotor to the tongue (**Figure 2.3E**). Some neurons in this region even innervated both the TA and the tongue (**Figure 2.3E**). Although the rv-iRF is distinct from brainstem sites that have previously been implicated in vocalization, such as the caudal RAm (Tschida et al., 2019), it is apparently unique in containing excitatory premotor neurons for multiple muscles of phonation. It therefore became the prime candidate for our proposed oscillator to pace and pattern neonatal cries.

The rv-iRF containing the premotor cluster is required for neonatal crying but not breathing.

We sought to test the necessity of the rv-iRF for patterning neonatal crying by measuring breathing and cries before and after bilateral electrolytic lesion of the premotor cluster medial to the cNA. Each animal's cry and breath parameters were measured 24 hours after lesion and normalized to pre-lesion data. The anatomical location of the lesions (along with other criteria, see methods section "stereotaxic electrolytic lesion") allowed us to classify them as bilateral on-target, bilateral off-target, or unilateral on-target (n = 5, 7 and 6, respectively). The lesions ranged approximately 100-200μm in diameter. On-target lesions were limited to the region medial to the cNA, in the location containing the common cluster of phonatory premotor neurons (**Figures 2.3** and **2.4B**).

Neonates with bilateral on-target lesions still attempted to vocalize (**Figure 2.4E**, ratio of post-lesion : pre-lesion cry bouts 0.86 ± 0.14 for on-target versus 1.08 ± 0.19 for off-target lesions, p = 0.2, t-test) by augmenting inspiratory and expiratory airflows (expiratory airflow: 0.89 ± 0.27 vs. 1.10 ± 0.07, p = 0.25 and inspiratory airflow: 0.92 ± 0.30 vs. 1.13 ± 0.13, p = 0.27), showing that

the rv-iRF is not the endogenous cry initiating signal. Instead, the breaths in each bout failed to produce normal cries and they commonly exhibited irregular airflow (compare **Figure 2.4A** with **2.4C**, **2.4E**). Bilateral on-target lesions resulted in a reduction in the number of unisyllabic and multisyllabic cries compared to off-target lesions (**Figure 2.4F**) and the few apparently normal augmented cry breaths were less likely to result in vocalizations (**Figures 2.4A**, **E-F**). Furthermore, the very scarce successful cries were abnormally short following on-target versus off-target lesions (**Figure 2.4H**). For each of these parameters, unilateral on-target lesions resulted in intermediate phenotypes (**Figures 2.4E-F**, **H**). Importantly, basal breathing frequency and regularity was unchanged in all lesioned animals (**Figures 2.4G** and **2.9**). Moreover, impaired crying in neonates with on-target lesions is unlikely to be attributed to the ablation of TA or CT motor neurons, which reside more caudal (>400μm) and/or ventral to the area of on-target lesions (Hernández-Morato et al., 2013; Patrickson et al., 1991), although we cannot definitively rule this out (**Figures 2.3C** and **2.11**). Indeed, even off-target lesions that partially included the cNA resulted in normal crying. Together, these data demonstrate that the patterning of neonatal cry bouts and the cries within a breath requires the rv-iRF, which contains premotor neurons for multiple phonatory muscles (**Figure 2.3**), but that the augmentation of cry breaths and normal breathing are independent of this proposed oscillator (**Figure 2.4I**).

The rv-iRF is sufficient to produce neonatal crying.

The necessity of the rv-iRF to produce the correct cry motor program indicates it plays either a 'central' or 'ancillary' role in patterning neonatal crying. We hypothesized that if selective activation of the rv-iRF could induce ectopic crying, it would implicate it as the core of the motor program. We stimulated the neonatal rv-iRF unilaterally with very short pulses of low amplitude

current that was incrementally increased (10ms train of 4 x 0.4ms biphasic pulses, starting at 50μA and up to 600 μA) while monitoring breathing and sound production. Surprisingly, in most animals, upon reaching a current threshold, the brief pulse reliably transformed basal breathing into an entire cry bout (**Figure 2.5A**, n=11/13 animals). After the recordings, the anatomical location of the electric stimulation was determined by the focal region of tissue damage. When low current amplitudes triggered cry bouts (≤ 150 μA), the targeted area resided within or immediately nearby (<150μm) the rv-iRF (on-target, n=8 animals). When significant current amplitudes were required to or failed to trigger a cry bout (>160-600 μA), the stimulated area was rostral or caudal to the rv-iRF (off-target, n=5 animals) (**Figure 2.5C**). The cry bouts after on-target stimulation started within ~200ms of the stimulus and were approximately normal in length (7.4 ± 0.8 breaths in stimulated vs. 9.7 ± 0.6 breaths in baseline recordings) (**Figure 2.5B**). Since the cry bouts last for several seconds beyond the 10ms electrical pulse, a dynamical and self-propagating system within the rv-iRF is likely engaged. And most importantly, this result, combined with the loss-of-function lesions, shows that the rv-iRF is a 'central' component in patterning neonatal cry (**Figure 2.5D**).

A novel oscillator in the rv-iRF is active during expiration.

We hypothesized that if the premotor cluster in the rv-iRF is the oscillator that controls fast rhythmic cries nested within a slower breathing pattern, its constituent neurons would oscillate faster than the preBötC inspiratory rhythm generator (Smith et al., 1991). We tested this idea using simultaneous recordings of ΔG-rabies-mCherry-positive TA premotor neurons in the rv-iRF and preBötC inspiratory activity in the hypoglossal nerve (cranial nerve XII) in medullary brainstem slices from neonatal mice (**Figure 2.6A**). Whole cell recordings of premotor neurons revealed a rhythmic oscillation of membrane potential throughout expiration (occurring every 6.2 ± 1.6 s),

which was faster than the rhythm of preBötC bursts (separated by 23.1 ± 1.8 s) (**Figures 2.6A, C, F**). To determine if this activity extends throughout the rv-iRF or perhaps beyond, we monitored the electrophysiological activity of a premotor neuron while simultaneously imaging GCaMP6s fluorescence emitted from all neurons in slices from *Snap25*-GCaMP6s transgenic mice (pan-neural expression of GCaMP6s) (**Figure 2.6A**). Only neurons located in an area directly medial to the cNA displayed synchronized rhythmic changes in fluorescence during expiration, coincident with the TA premotor neuron activity (**Figure 2.6B**). The synchronicity of the rhythmic activity was validated by paired whole cell recordings (**Figure 2.6D**) and the rhythmic activity was even synchronized bilaterally (**Figure 2.6E**). This region precisely coincided with the rv-iRF containing the vocalization phonatory premotor neurons, lesions of which nearly eliminated cries and upon stimulation induced ectopic cries (**Figures 2.4** and **2.5**). We named this cluster of dozens of neurons the intermediate reticular oscillator (iRO, **Figure 2.6B**).

Moreover, when fast synaptic communication between neurons was prevented with a cocktail of synaptic transmission blockers (10 μM NBQX, 50 μM APV, 100 μM picrotoxin, and 1 μM strychnine), all the iRO neurons retained synchronous rhythmic oscillations in electrical activity and *Snap25*-GCaMP6s fluorescence (**Figures 2.6F** and **2.13A-C**). This uniquely defining feature further distinguished them from other nearby neurons and the preBötC (**Figures 2.6F** and **2.13B**). This iRO oscillatory activity was found in ΔG-rabies-traced TA (**Figure 2.13A**), CT, and tongue premotor neurons (**Figure 2.12A**) in the area, but not premotor neurons for other orofacial oscillators (**Figure 2.12B**) or respiratory centers in the brainstem (**Table 2.1**). For example, although PiCo is anatomically nearby or perhaps overlapping, iRO is molecularly and electrophysiologically distinct (see discussion) (Anderson et al., 2016). We thus concluded that

the iRO is a novel oscillatory node within the medullary brainstem, and it is uniquely composed of premotor neurons for multiple muscles of vocalization.

We next investigated the mechanism underlying the oscillatory behavior of iRO neurons. In the presence of our cocktail of synaptic transmission blockers, each iRO neuron displayed a rhythmically-timed inward current when the membrane potential was clamped at -80 mV, which was eliminated by the gap junction antagonists carbenoxolone (Cbx), 18ß-glycyrrhetinic acid, and meclofenamic acid (**Figure 2.13F**). Furthermore, the rhythmic activity in an iRO neuron persisted when voltage-gated sodium channels were blocked only within the patched neuron but was abolished when these sodium channels were blocked in nearby neurons (**Figure 2.13D**). And lastly, the iRO neurons showed direct electrical coupling (**Figure 2.13E**). These data affirm that iRO neurons are coupled by gap junctions and that this, rather than fast synaptic signaling, is required for the autonomous oscillatory behavior that is unique to the iRO.

Using depolarizing and hyperpolarizing neuromodulators, we subsequently revealed that the iRO rhythm ceased upon network hyperpolarization and was therefore voltage dependent (**Figures 2.14A-B**). This conditional rhythmic activity is consistent with the intermittent nature of crying. By analogy with other voltage-dependent rhythms, we predicted that at least three different currents would give rise to the interburst interval, the burst, and its termination. The canonical I_h pacemaker current carried by hyperpolarization-activated cyclic nucleotide-gated channels (Kaupp and Seifert, 2001) was not involved in setting the interburst interval (100µM ZD7288). However, block of the depolarizing persistent sodium current I_{NaP} eliminated the rhythm (20µM riluzole, **Figure 2.14E**), consistent with a role in setting the interburst interval, burst, or both (French et al.,

1990; Yamanishi et al., 2018). Bursting was attenuated or prolonged by blocking or augmenting L-type calcium channel (LTCC) activity, respectively (2μM nifedipine and 100nM Bay K8644, **Figures 2.14C-D**), but was not affected by a T-type calcium channel antagonist (10μM mibefradil). Surprisingly, burst termination was not affected by any of the calcium-activated potassium channel antagonists that we tested (50nM IbTX, 50nM UCL1684), but was altered by preventing voltage-gated sodium channel inactivation (250nM veratridine, **Figure 2.14F**).

While iRO can oscillate independently from the preBötC (**Figure 2.6F**), the pharmacological profile provided an opportunity to determine if antagonizing the iRO rhythm impacted the preBötC. *In vitro,* bath application of the gap-junction (Cbx) or LTCC (nifedipine) blockers did not change the preBötC rhythm, thereby demonstrating these two oscillators are distinct (**Figures 2.6G-H**). Next, to determine the requirement of the iRO rhythm for patterning cries, we measured breathing and vocalizations before bilaterally injecting the iRO with either Cbx or nifedipine, then remeasured breathing and vocalizations. Injection of Cbx or nifedipine did not change the number or length of cry bouts but decreased the number of breaths with vocalizations in a cry bout and unisyllabic cry length, and appeared to only somewhat reduce the proportion of cries with multiple syllables due to large variance in this parameter (**Figures 2.15A-C**). In contrast, injection of ACSF as a control only minimally decreased the number of breaths containing vocalizations within a cry bout and did not change the proportion of multisyllabic cries nor the length of unisyllabic cries (**Figures 2.15A-C**). Consistent with our *in vitro* studies, basal breathing was unchanged by Cbx or nifedipine (**Figures 2.15C** and **2.9**). The changes observed in cries after pharmacologically antagonizing the iRO rhythm appear similar to those produced by electrolytic lesions, and thus

demonstrated that the iRO's intrinsic rhythm is likely required for patterning neonatal cries within the breath, consistent with it being the proposed cry oscillator.

The iRO recruits the preBötC and laryngeal motor neurons to produce the cry motor program.

The first feature of the cry motor program is the activation of inspiratory muscles that precedes the onset of each cry syllable (**Figure 2.2**). We postulated that the iRO triggers the inspiratory motor program via the preBötC (**Figure 2.7A**). *In vitro*, ~50% of recorded preBötC neurons displayed excitatory postsynaptic potentials (EPSPs) coincident with each iRO oscillation and these disappeared after antagonizing the iRO rhythm with carbenoxolone (**Figures 2.7B-C**). This suggests an excitatory connection (direct or indirect) from the iRO to the preBötC. Furthermore, preBötC bursts, coincident with hypoglossal nerve root activity (**Figures 2.7D-E**, black), occurred in phase with, or immediately after, the onset of iRO oscillations (**Figure 2.7C** - note the consistent iRO oscillation in the PSTH preceding the preBötC burst; and **2.7D** – compare the similar intervals between iRO to iRO and iRO to preBötC), showing that the iRO biases the timing of preBötC bursts. Combined, these data demonstrate a physical and functional coupling of the iRO and preBötC rhythms. Thus, the iRO has the connectivity necessary to initiate the inspiratory motor program that precedes each of the cry syllables within a breath. Note, although unlikely, we cannot eliminate a possible third center that simultaneously excites both the iRO and preBötC.

The second key feature of the cry motor program is the laryngeal adduction to produce sound that follows each inspiratory event, known as post-inspiratory activity (Riede, 2014) (**Figure 2.7F**). In contrast to preBötC neurons, the excitation of iRO neurons during inspiration persisted through

post-inspiration (**Figure 2.7G**). Because iRO neurons are glutamatergic and premotor to laryngeal adductors (**Figures 2.3** and **2.11**), their post-inspiratory activity is consistent with the ability to generate cries. However, an additional mechanism must be invoked to explain the prevention of laryngeal adduction during inspiration. We investigated this using voltage-clamp recordings of TA motor neurons *in vitro* following their identification by intramuscular injection of Alexa Fluor 555-conjugated cholera toxin B (**Figures 2.7H-I**). Nearly all recorded TA motor neurons exhibited inhibitory synaptic currents during each inspiration, and 60% displayed excitatory post-inspiratory activity, which we expected to result from the iRO activity (**Figure 2.7H**). These excitatory and inhibitory inputs were also evident during each iRO oscillation (n = 12/22 motor neurons) (**Figure 2.7H**, red arrows). This *in vitro* activity mirrors the timing of laryngeal sound production during each cry syllable.

Blockade of excitatory synaptic transmission (using 10 μM CNQX and 50 μM APV) silenced the preBötC (Smith et al., 1991) and even eliminated all inhibitory synaptic modulation of TA motor neurons (**Figure 2.7I**). As iRO remains rhythmic in this condition (**Figures 2.6** and **2.13**), the direct inhibitory input to TA motor neurons must therefore be from a different source, likely the Vgat-positive TA premotor neurons within the preBötC or RAm (**Figure 2.3**). Upon blockade of inhibitory synaptic transmission (using 100 μM picrotoxin and 1 μM strychnine), excitatory synaptic input remained and it accurately mimicked the iRO activity, as expected (**Figure 2.7H** vs. **7I**). This connectivity between the iRO, the inhibitory inspiratory neurons, and TA motor neurons comprises a plausible mechanism by which the iRO patterns post-inspiratory laryngeal adduction and sound production. Thus, by recruiting the preBötC to drive the inspiratory motor

program and directly activating laryngeal adductors post-inspiration, the iRO could pattern neonatal cries.

Optogenetic excitation of the iRO induced neonatal cry bouts and added an additional syllable.

The retention of synchronous rhythmic activity in synaptic blockers allowed us to screen fourteen Cre recombinase lines that might label the iRO (Cre > GCaMP6f, **Table 2.1**). The screen validated that the iRO is composed of only excitatory neurons (like **Figure 2.3**) and identified expression of two neuropeptides, *Penk* and *Tac1*. Co-expression of Vglut2-Flp and Penk-Cre labeled neurons within the iRO region (**Figure 2.8A**), and electrophysiological recordings of these neurons in synaptic blockers showed they were indeed the iRO (**Figure 2.8B**, n = 5/7 neurons). We could robustly depolarize the iRO neurons with light after expression of the ReaChR opsin with Vglut2-Flp and Penk-Cre (Vglut2-Flp; Penk-Cre > LSL/FSF ReaChR) (**Figure 2.8B**). Quantification of Vglut2-Flp; Penk-Cre > ReaChR neurons throughout the ventrolateral medulla showed numerous neurons within the iRO and some labeling within the PiCo (only 23% of *ChAT*-expressing cells), the BötC, preBötC, and RAm (**Figure 2.8C**). The ability of ReaChR to depolarize the iRO, coupled with its expression pattern and careful fiber optic placement, offered the ability to ectopically activate the iRO *in vivo* during basal breathing and ongoing cries.

Triple transgenic neonates were unilaterally implanted with an optic fiber above or adjacent to the iRO and we ectopically activated the iRO with 1 to 2 seconds of 10Hz light during basal breathing. In most instances, several breaths were augmented, appearing similar to cry breaths (**Figure 2.8D**, 2.22 ± 0.48 breaths, 9 / 9 $ReaChR^+$ animals vs. 0.16 ± 0.09, 3 / 5 WT, p-value = 0.001). Remarkably,

in many cases basal breathing was transformed into a complete cry bout that persisted beyond the light pulse (**Figure 2.8E**, 5 / 9 animals), mirroring the effect of the rv-iRF electrical stimulation (**Figure 2.5**). The cry bouts started 2.1±0.9 seconds after the laser onset (0.6±0.9 seconds after laser offset) and appeared similar to endogenous cry bouts in length, 10.6 ± 0.7 breaths versus 9.7 ± 0.6 (**Figure 2.8F**). Cry bouts never occurred in wildtype controls after light pulses (**Figure 2.8F**, n = 5 animals). Since optogenetic activation of the iRO mimics the effect of localized electric stimulation of the rv-iRF, it is unlikely that the induced cry bouts result from activation of ReaChR$^+$ neurons in other areas such as RAm. The sufficiency of the iRO to drive an ectopic cry bout is consistent with it playing a central role in patterning neonatal cries.

Next, we hypothesized that stimulation of the iRO with a triggered, single 50ms light pulse during or immediately after the first cry syllable within a breath would induce a second syllable (**Figure 2.8G**). This is indeed the case. Quantification of cry syllables (ultrasonic sound or the expiratory airflow peak that accompanies a syllable) showed an enrichment of bisyllabic cry breaths after light stimulation compared to a similarly triggered sham stimulation (**Figure 2.8G**, ratio of light : sham = 1.7 ± 0.17, n = 9 animals). No difference was observed in control animals (light : sham = 0.97 ± 0.04, n = 6 animals, p-value ReaChR$^+$ vs. control = 0.001) (**Figure 2.8G**) and basal breathing was unchanged by the 50ms light pulse (**Figures 2.8H**, **2.16**). In summary, these optogenetic data demonstrate that activation of the iRO is sufficient to pattern the cry syllables within a breath and even sufficient to pattern entire cry bouts (**Figure 2.8I**).

DISCUSSION

We have identified a novel brainstem node, the iRO, which acts as an autonomous oscillator that organizes the patterning of neonatal mouse vocalizations with breathing. Its proximity to the cNA is consistent with a previous hypothesis that a central pattern generator for vocalization resides in the medullary reticular formation (Hage, 2009). A simple model predicts that patterning of laryngeal and breathing motor groups is sufficient to control vocalizations (Zhang and Ghazanfar, 2020). Furthermore, it is anticipated that such a patterning system would also encode the tempo of syllables within vocalizations. Our results are consistent with such a model.

The iRO produces a conditional and flexible rhythm to time syllables.

The iRO rhythm requires gap junctions but not synaptic neurotransmission (**Figure 2.6**). Additionally, the speed of the rhythm can be tuned by membrane potential of the iRO network (**Figure 2.14**). In this way, electrical coupling integrates the membrane properties of all the iRO neurons, some of which may be intrinsic pacemakers, resulting in a robust, voltage-dependent, and tunable rhythm. Such a rhythm is to be expected for neonatal cries since they come-and-go in bouts, and the number of syllables within a cry breath is flexible, necessitating a conditional and tunable oscillator. In this model, the iRO would be most depolarized and oscillating fastest mid-bout, consistent with when we observe the most multisyllabic cries. Interestingly, momentary stimulation of the iRO triggers a prolonged cry bout (**Figures 2.5** and **2.8**). One hypothesis is that this occurs because the iRO is a dynamical and self-propagating system, the mechanisms of which will be an interesting area of future study. Note, the different speeds of the iRO *in vitro* and syllables *in vivo* is likely due to less excitable conditions *in vitro* (temperature and solutions) and removal of inputs in the slice. This is just like the much slower inspiratory preBötC rhythm *in vitro*

compared to breathing rates *in vivo*. Yet, given the changes in neural dynamics *in vivo* and the technical challenges of the *in vivo* pharmacological experiments we conducted (**Figure 2.15**), further tests are needed to confirm if the intrinsic iRO rhythm *in vitro* is required to pattern neonatal cries.

The iRO patterns the motor sequence to produce multisyllabic cries.

To our surprise, the motor pattern of multisyllabic neonatal cries is the fast recycling of the normal breath sequence – inspiratory activity followed by post-inspiratory laryngeal adduction (**Figure 2.2**). In our model, iRO re-activates the preBötC, and thus inspiratory muscles, during the expiration of a cry breath. The opposing inspiratory force causes a dip in airflow that forms the gap between syllables. Each "inspiratory" dip is then followed by the natural post-inspiratory laryngeal adduction to produce sound. *In vitro*, the iRO has the connectivity to produce this entire motor sequence (**Figure 2.7**).

An alternative model for generating a multisyllabic cry involves an oscillator that rhythmically drives multiple forced expirations within a breath. In this model, the gaps between syllables would simply be brief pauses in expiration. However, this is not the case. While we cannot rule out that active expiration may also participate in generating neonatal cries, our data necessitates that the interval between syllables originates from a re-activation of the inspiratory motor program, rather than a pause in expiration. To our knowledge, this is the first instance that inspiration has been shown to be ectopically re-activated during expiration leading to a nested rhythm within breathing.

iRO fulfills the criteria to be a central pattern generator used in vocalization.

Central pattern generators (CPGs) are critical for making rhythmic and stereotyped motor sequences like chewing and walking. To be classified a CPG, a collection of neurons must autonomously produce a rhythm and also encode a motor pattern (Grillner and El Marina, 2020, Marder and Bucher, 2001). The iRO's intrinsic rhythm throughout expiration, its synaptic bilateral synchronization, the connectivity to coordinate inspiratory and laryngeal muscle activity, the necessity of it and its rhythm for neonatal cries, and its sufficiency to produce complete cry bouts and cry syllables fulfill the key criteria to define the iRO as a CPG used in vocalization. Importantly, lesion of the iRO impacts the motor pattern of cries, but not the number of attempted cry bouts, and stimulation during a cry can produce an extra syllable, demonstrating it is not simply an upstream cry initiation signal. And surprisingly, unlike other well characterized CPGs, the same iRO neurons participate in both pacing and patterning. Our chosen *in vivo* approaches were influenced by the technical limitations of neonatal studies (e.g., absent AAV gene expression in several days), thus, although each experiment has caveats (e.g., electrolytic lesions of passing fibers or optogenetic excitation of nearby $Vglut2^{+}Penk^{+}$ neurons), the diversity of experiments with a unified impact upon cries (necessity: lesion / pharmacology and sufficiency: electrical / optogenetic stimulation) has led us to the parsimonious model that the iRO patterns neonatal cries.

The midbrain periaqueductal gray (PAG) and the medullary nucleus tractus solitarius (NTS) are two additional brainstem sites implicated in vocalization (Tschida et al., 2019 and Hernandez-Miranda et al., 2017). Each region projects to expiratory and laryngeal motor neurons in the medullary retroambiguus (RAm) and are required for murine ultrasonic vocalizations. Here, we propose that the iRO is downstream of both the PAG and NTS and serves to pattern the breaths in

a cry bout and the vocalizations within each breath. Also, we predict that the PAG and NTS input to RAm serves to augment airflow during the cry since the iRO lesions primarily alter the cry breath structure (**Figure 2.4**). Nonetheless, since activation of the iRO can induce complete cry bouts, the iRO must also be sufficient to augment expiratory airflow (**Figures 2.5** and **2.8**).

Is the iRO a component of the nearby respiratory centers?

The iRO is anatomically nearby or overlapping with the vital inspiratory rhythm generator (the preBötC) and the Postinspiratory Complex (PiCo) (Del Negro et al., 2018). Is it therefore a component of one or both respiratory centers? For example, although the iRO displays preBötC inspiratory activity, the iRO activity persists through postinspiration (**Figure 2.7**), the iRO nor its intrinsic rhythm are required for the preBötC to pace inspiration (**Figure 2.6**), and the iRO is localized rostral / medial to the preBötC core (**Figures 2.4, 2.6,** and **2.11**). Compared to PiCo, the iRO does not possess the many defining molecular or electrophysiological properties (e.g., ChAT-Cre lineage, restricted postinspiratory activity, norepinephrine- and synapse-dependent rhythm, non-Dbx1 derived) (Anderson et al., 2016); however, the iRO markers *Vglut2*$^{+}$/*Penk*$^{+}$ were found in 23% of ChAT-expressing neurons in the area.

Also, we refrained from calling the iRO a component of the preBötC or PiCo since it appears to have a very specific role in neonatal vocalizations but not basal breathing. The iRO is not required for the basal breathing pattern (**Figures 2.4, 2.9**) nor does momentary activation of the iRO shift the phase of a basal breath (**Figures 2.8, 2.16**, an expected forward phase shift for preBötC or backward for PiCo). These are each key features of both these respiratory centers. Consistently, cries were disrupted by two approaches to pharmacologically antagonize the iRO rhythm that do

not impact these other respiratory oscillators. Since the iRO does not strictly follow the canonical definitions of either the preBötC or PiCo, we named this collection of neurons based on its anatomical localization and physiological characteristic; however, future studies will be needed to definitively determine whether the iRO is functionally distinct or is a subset of the preBötC and PiCo. Other important future studies will be to understand the interactions of these centers, like does the preBötC re-time the iRO rhythm or does PiCo drive the iRO post-inspiratory activity?

The medullary brainstem is packed with separate but interacting patterning systems that control behaviors like whisking, swallowing, and breathing (Del Negro et al., 2018), and we now add crying / vocalization as a novel behavior to this list.

FIGURES

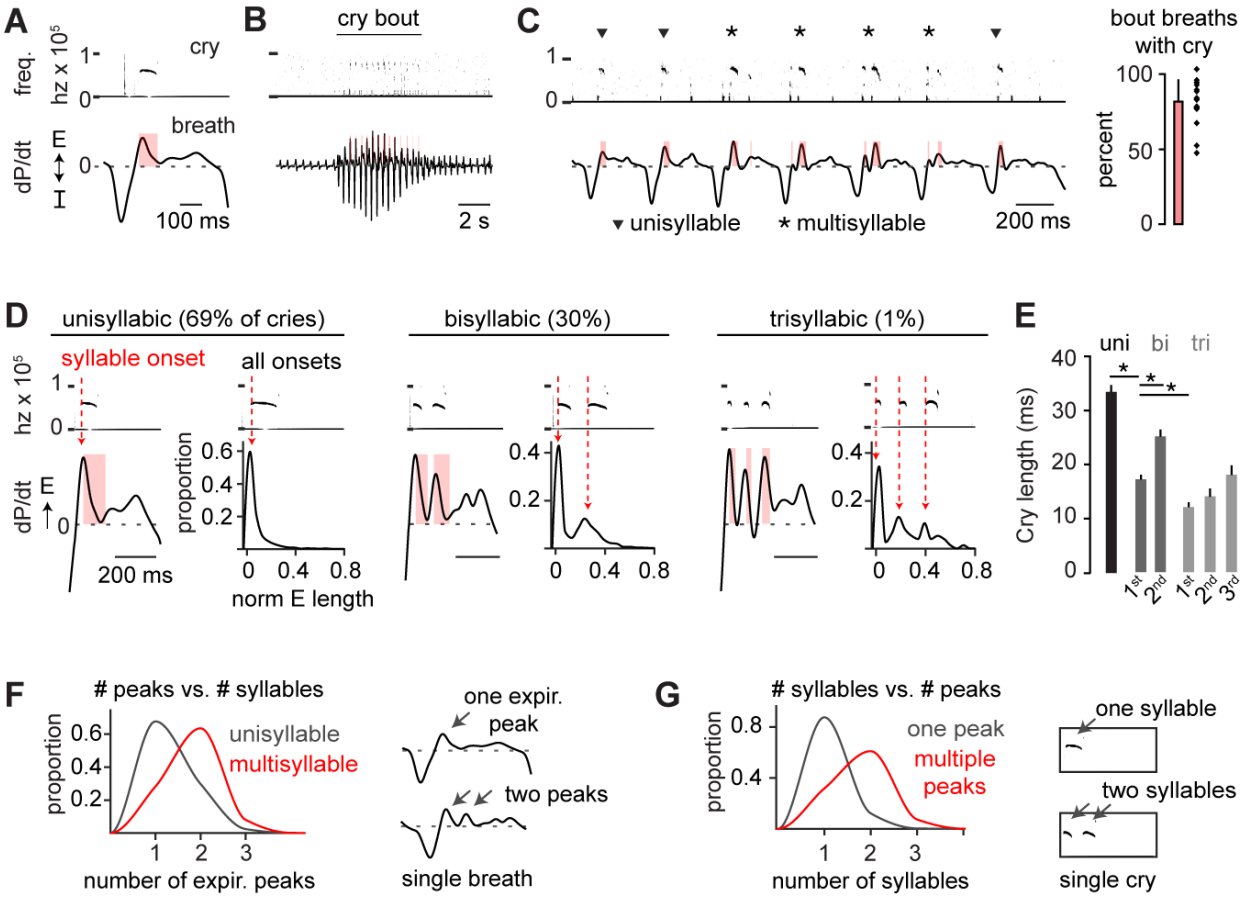

Figure 2.1. Neonatal cries comprise syllables that are rhythmically timed within a breath.

A, Example cry breath with associated cry (frequency spectrogram 0-100 kHz) and respiratory pressure changes (dP/dt, arbitrary units). E and I, expiratory and inspiratory pressure change. Red bar indicates USV length. **B**, Example of large breaths during a cry bout and basal breaths before and after. **C**, Enlargement of cry bout in **B** showing four multisyllabic (*) and three unisyllabic (▾) cries. Right, proportion of large cry bout breaths with cries (n = 17 mice, mean + SD). **D**, Left, representative examples of expiratory airflow when one, two, or three syllables are voiced within a single breath. Right, histograms of cry onset time normalized to expiratory duration (total n = 5596 cries from n = 23 mice). **E**, Syllable length within uni-, bi-, and trisyllabic cries. *, one-sided t-test p-value < 0.05. **F**, Proportion of expiratory peaks in cry breaths that contain one (uni-) versus two or more (multisyllable) cries (n = 11,186 cry-breaths, from n = 30 mice). **G**, As in **F**, but the proportion of syllables in cry breaths with one or multiple expiratory airflow peaks.

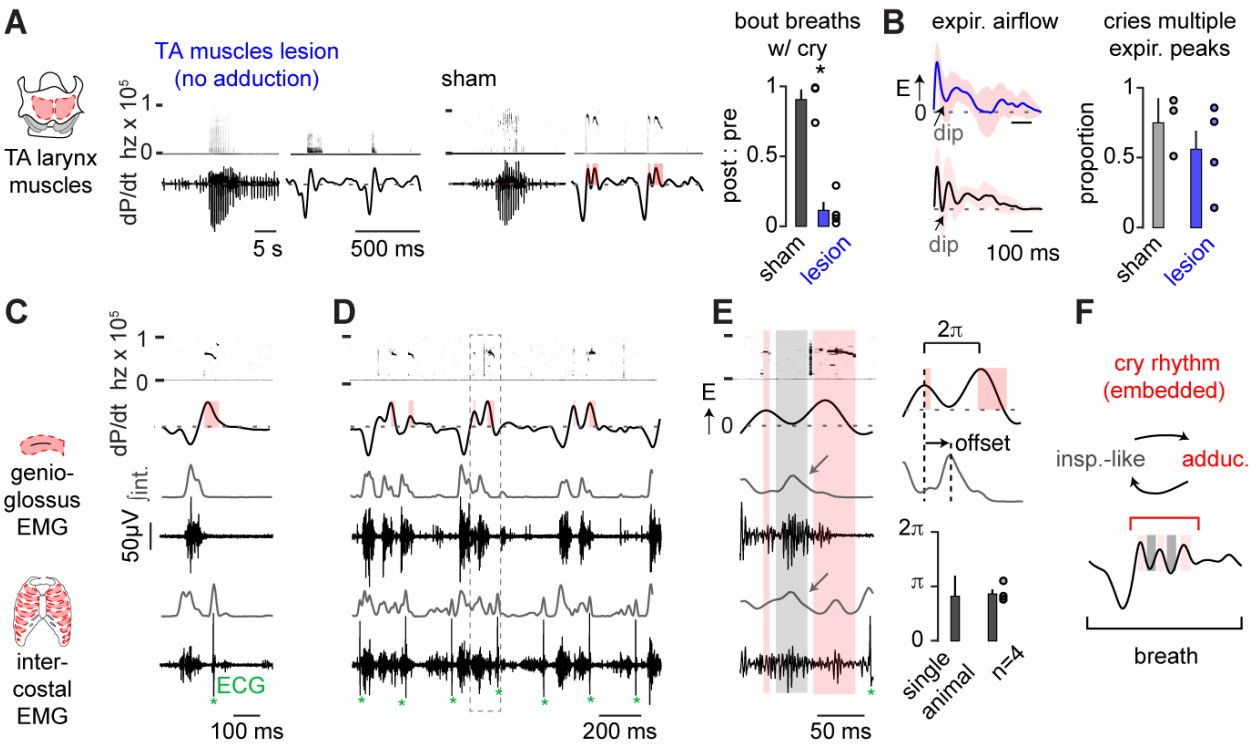

Figure 2.2. Cry syllables are synchronized with the respiratory motor program.

A, Example cry bout and three cry breaths after bilateral electrolytic lesion of the TA laryngeal adductor muscle (left) and sham lesion (middle). Right, the number large cry bout breaths with cries in post- versus pre-surgery (post:pre) recordings. Sham, black, n = 3; TA lesion, red, n = 4; mean ± SEM. *, one-sided Wilcoxon rank sum p-value < 0.05. **B**, Average ± SD of cry breath expiratory airflow after TA lesion (n=47 breaths for lesion and n=26 sham) and proportion of cry breaths with multiple expiratory airflow peaks in sham and lesioned animals (average ± SEM, ~70 breaths analyzed per animal lesioned and ~100 per sham). Breaths retain airflow oscillations reminiscent of multisyllabic cries after TA lesion. **C**, Electromyographic (EMG) activity of the genioglossus (n = 4) and intercostal (n = 5) inspiratory muscles. Gray, integrated (∫int.) activity. Example unisyllabic cry and associated inspiratory muscle activity. * denotes contaminating cardiac ECG signals. **D**, Example multisyllabic calls with additional inspiratory activity during airflow dips. **E**, Left, example multisyllabic cry breath from boxed region in **D** showing the gap between syllables coinciding with genioglossus and intercostal activity. Right, quantification of timing of genioglossus activity with respect to peak expiratory airflow for a single neonate and n = 4 animals. **F**, Schematic showing how cycling of inspiration and laryngeal adduction produces multisyllabic cries within a slower breathing rhythm.

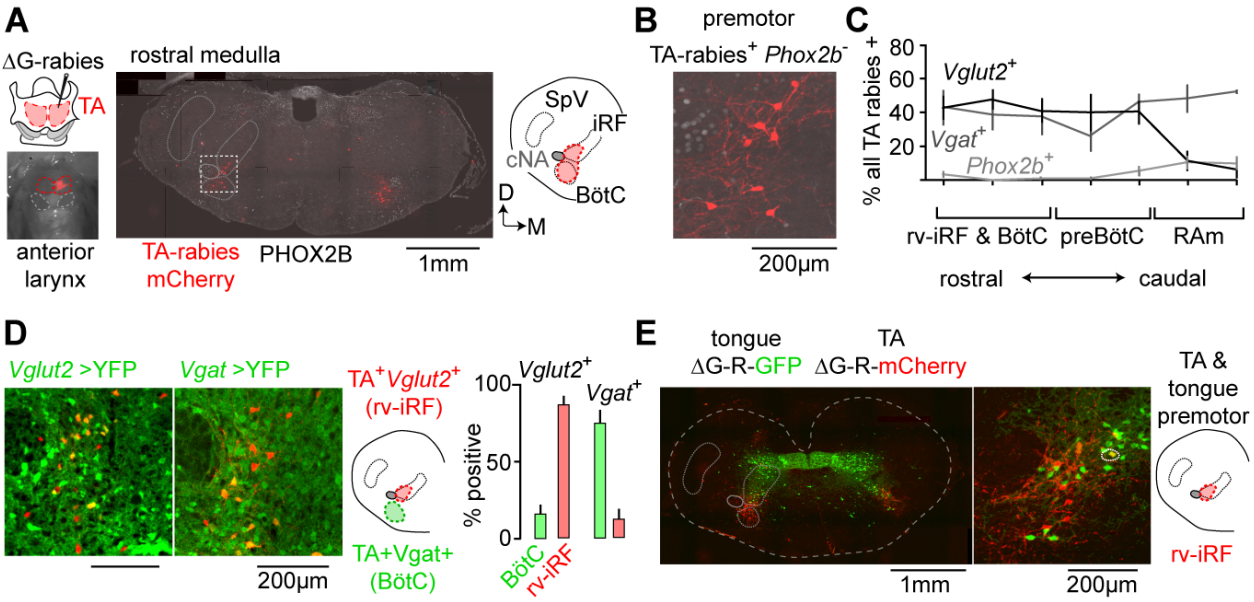

Figure 2.3. The medullary brainstem contains a cluster of premotor neurons for sound production and articulation.

A, Monosynaptically-restricted rabies virus injected into the TA (ΔG-Rabies-mCherry and HSV-G). Middle, 20μm thick slice of the rostral medullary brainstem showing the distribution of rabies-mCherry-positive TA premotor neurons (red) and Phox2b expression (gray). Right, schematic of slice illustrating the position of the iRF and BötC, cNA, and spinal trigeminal nucleus (SpV). D, dorsal; M, medial. **B**, Left, magnification of boxed area in **A** showing a cluster of Phox2b-negative premotor TA-traced neurons directly medial to the cNA. **C**, Quantification of the mean percent ± SEM of rabies-infected neurons that were *Vglut2*-positive (black, n=3), Vgat-positive (gray, n=3), or Phox2B-positive (TA motor, pale gray, n=6) across the ventral respiratory centers (rv-iRF/BötC, preBötC, and RAm). **D**, Left, TA premotor neurons in the rv-iRF and BötC of Vglut2-Cre→YFP (n=3) and Vgat-Cre→YFP mice (n=3). Neurons medial to cNA are *Vglut2*-positive (rv-iRF) and those in ventral BötC are Vgat-positive. Right, quantification. **E**, Left, Slice of the rostral medullary brainstem showing the distribution of ΔG-rabies-mCherry-positive TA premotor neurons and ΔG-rabies-GFP-positive tongue premotor neurons. Middle, magnification of rv-iRF showing spatial overlap of TA and tongue premotor neurons. Circled neuron is double positive. Right, schematic of slice illustrating the position of the rv-iRF.

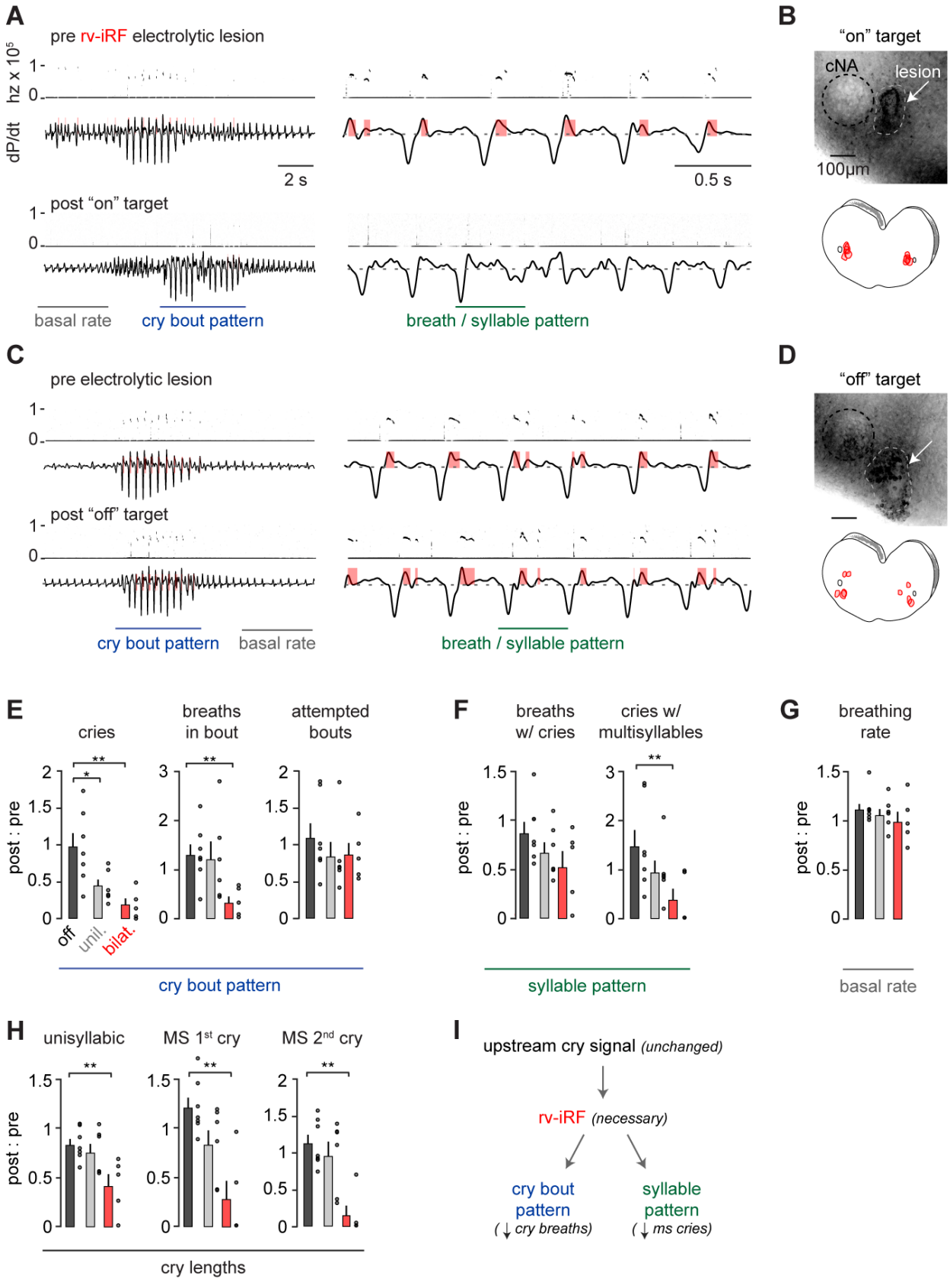
A
pre rv-iRF electrolytic lesion
hz x 10⁵
dP/dt
2 s
0.5 s
post "on" target
basal rate
cry bout pattern
breath / syllable pattern
B
"on" target
cNA
lesion
100µm
C
pre electrolytic lesion
post "off" target
cry bout pattern
basal rate
breath / syllable pattern
D
"off" target
E
cries
breaths in bout
attempted bouts
post : pre
off
unil.
bilat.
cry bout pattern
F
breaths w/ cries
cries w/ multisyllables
syllable pattern
G
breathing rate
basal rate
H
unisyllabic
MS 1st cry
MS 2nd cry
cry lengths
I
upstream cry signal (unchanged)
rv-iRF (necessary)
cry bout pattern
(↓ cry breaths)
syllable pattern
(↓ ms cries)

Figure 2.4. The rv-iRF premotor cluster is required for neonatal crying but not breathing.

A, Representative cry bout and breathing pattern before (top) and after (bottom) bilateral on-target electrolytic lesion of the rv-iRF medial to cNA. **B**, Top, representative light microscopy image of the lesion. White arrow indicates lesion site. Bottom, summary of locations for all on-target lesions (n=5). **C-D**, As in **A-B** but for off-target lesions (n=7). **E**, Quantification of number of cry bouts and the breaths and cries within them following bilateral on-target (Bilat.), unilateral on-target (Unil., n=6), and off-target (Off) electrolytic lesions. Each parameter is represented as a ratio of post-lesion : pre-lesion. Parameters include: the total number of unisyllabic and multisyllabic (MS) cries ($p = 0.002$), number of cry breaths in a bout ($p = 0.002$), and number of cry bouts in 5 minutes ($p = 0.2$). **F**, As in E, where each parameter represents a feature of the cry breath pattern: the number of large breaths in a cry bout with a vocalization ($p = 0.08$), proportion of cries that are MS ($p = 0.006$). **G**, Basal respiratory rate ($p = 0.1$). **H**, Length of each cry syllable ($p = 0.01$, 0.004, 0.002). Data are mean ± SEM. One-sided t-test or Wilcoxon rank sum P-value < 0.05 (*) and < 0.01 (**). **I**, Model indicating that the rv-iRF is necessary for patterning the cry bouts and breaths within them.

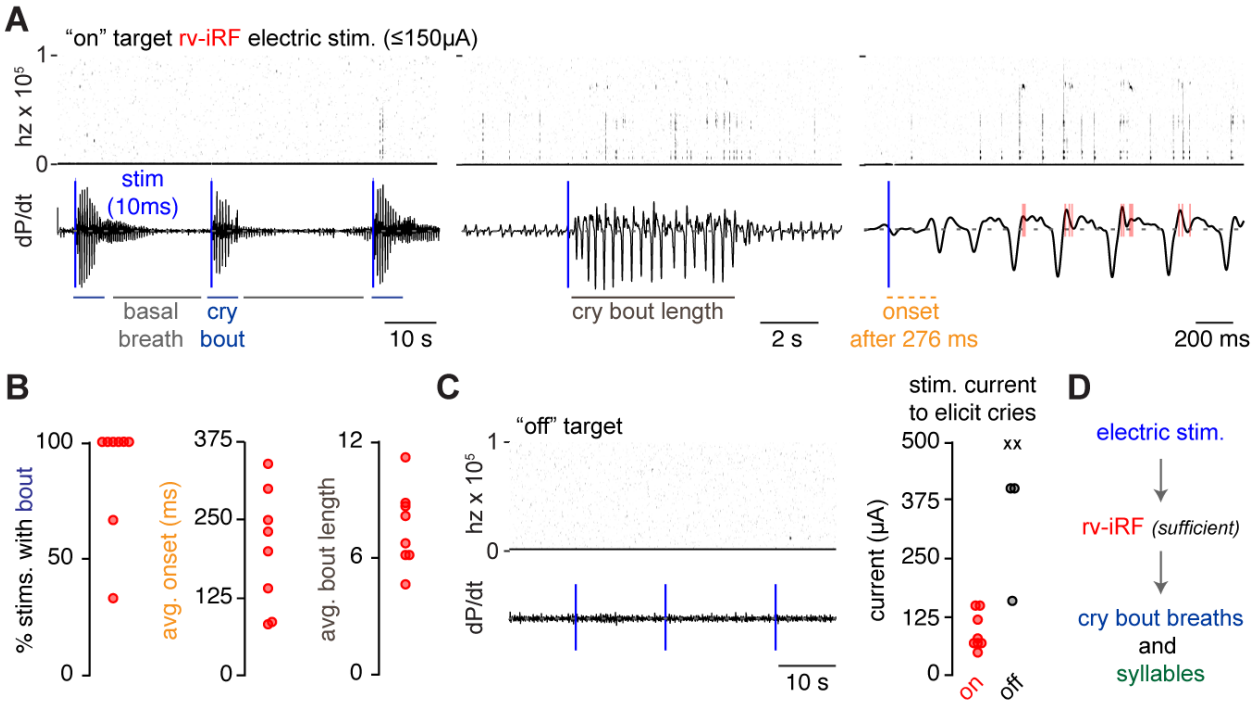

Figure 2.5. The rv-iRF is sufficient for neonatal crying.

A, Representative airflow and ultrasonic sound recordings with three unilateral on-target 10ms electrical stimulations (4 x 0.4ms biphasic pulses). On-target stimulations required ≤150μA of current. Middle, example cry bout following electrical stimulation. Right, example cry breaths after electrical stimulation. Blue vertical line indicates 10ms stimulation. **B**, Quantification of the percent of on-target stimulations that triggered a cry bout at ≤150μA in each animal, average time to cry bout onset after electric stimulation, and average bout length. **C**, Left, representative airflow and ultrasonic sound recordings with three 10ms electrical stimulations in an off-target electrical stimulation that failed to elicit any cry bouts. Right, amount of current (μA) required to initiate a cry bout when the stimulation is on (red circle, n=8 animals) or off-target (black circle or X, n=5). X, denotes animals where all tested currents up to 600μA failed to elicit cries (n=2). **D**, Model indicating that the rv-iRF is sufficient to induce the entirety of a cry bout.

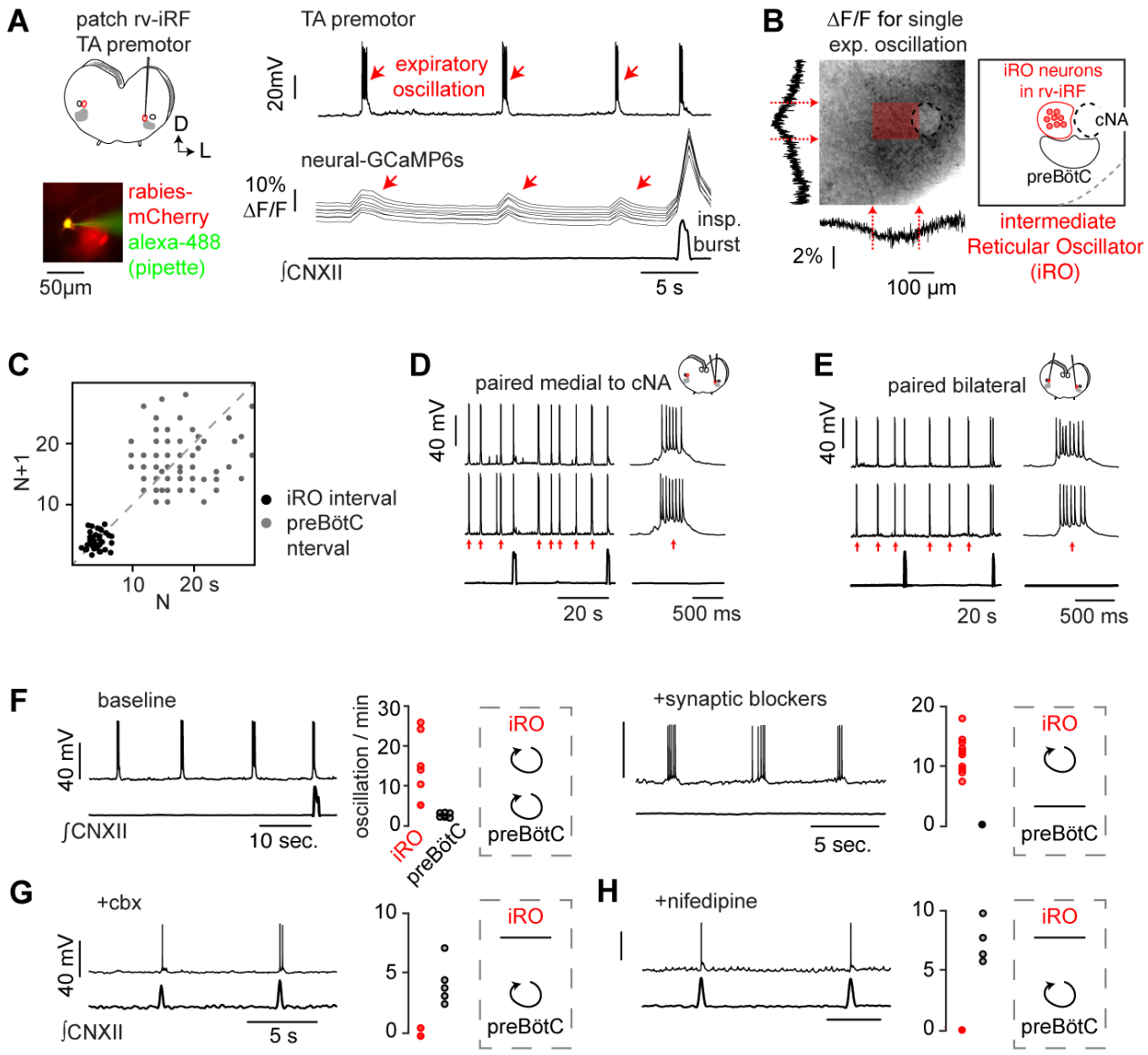

Figure 2.6. A novel oscillator in the rv-iRF is active during expiration.

A, Left, medullary *in vitro* slice preparation. preBötC inspiratory rhythm monitored via cranial nerve XII (∫CNXII) and ΔG-rabies-mCherry TA premotor neurons in rv-iRF recorded using patch clamp (bottom, filled with Alexa-488 from pipette). Right, current clamp (I_c) recording of TA premotor rv-iRF neuron (n = 17/20), ΔF/F in 10 neurons (*Snap25*-GCaMP6s), and ∫CNXII. Red arrows indicate expiratory oscillation. **B**, ΔF/F summed vertically and horizontally during a single expiratory oscillation (dashed box, left). ΔF/F localizes to dozens of neurons medial to cNA, denoted by shaded red box, which we named the iRO. **C**, Left, Poincaré plot of iRO (black) and preBötC (gray) intervals. **D**, Paired I_c recordings of rv-iRF neurons medial to cNA. Neurons show a synchronous expiratory oscillation. **E**, As in **D** but bilateral. **F**, I_c recording of iRO neuron and

∫CNXII and mean ± SEM of oscillations per minutes (n=6 slices) before (left) and after bath applied blockers of fast synaptic neurotransmission (10µM NBQX, 50µM APV, 100µM Picrotoxin, 1µM Strychnine, n=10) (Right). Only iRO rhythmic activity persists and is synchronous. **G-H**, As in **F**, but after bath application of 50µM carbenoxolone (**G**, n=5) or 2 µM nifedipine (**H**, n=4). The iRO expiratory rhythm is abolished in both cases, but not the preBötC.

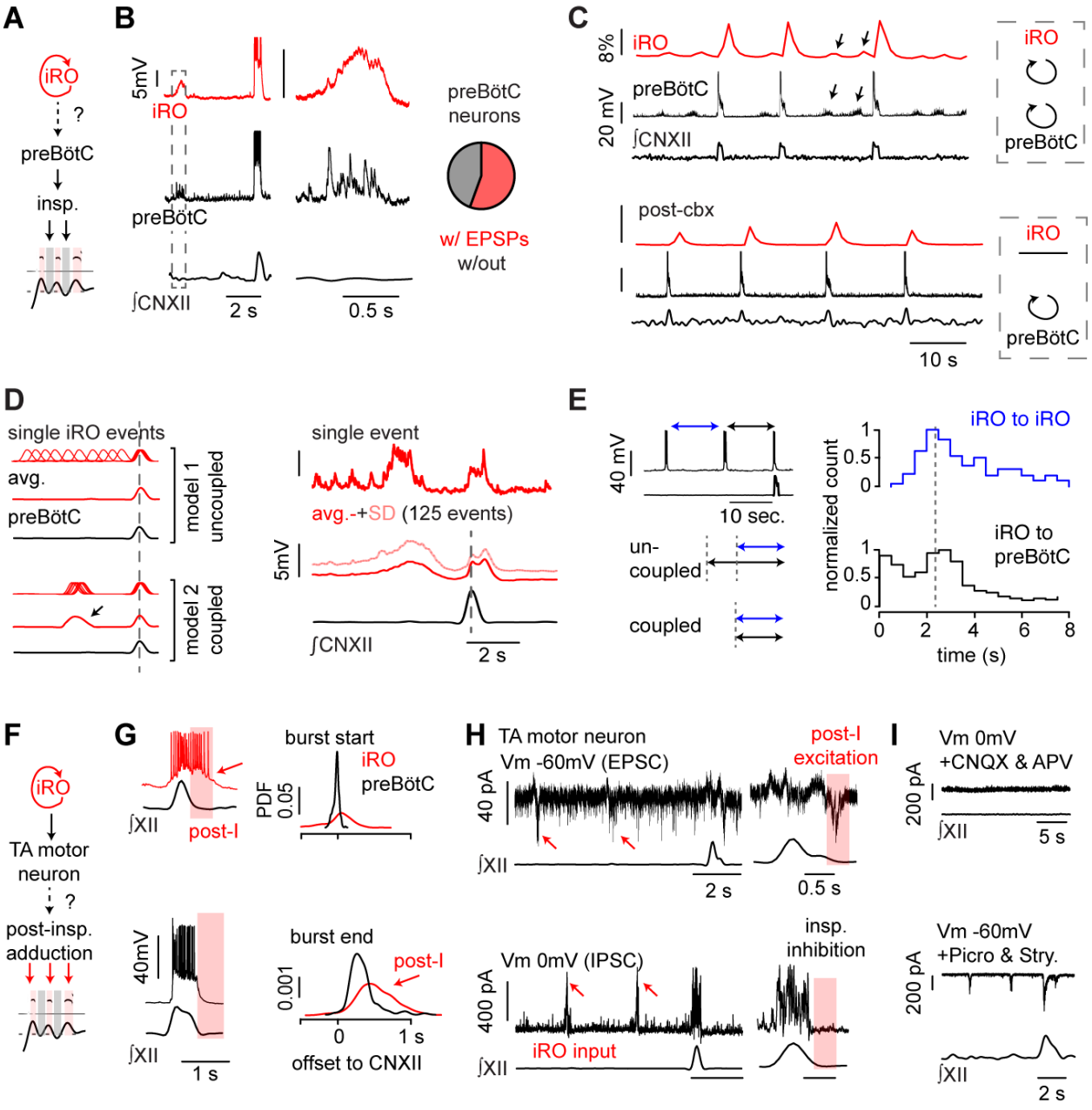

Figure 2.7. The iRO uses synaptic and functional connections to produce the cry motor program.

A, Schematic of iRO control of inspiration (**Figure 2.2**). **B**, Left, paired I_c recordings of iRO and preBötC inspiratory neurons (n = 5/11 paired recordings). PreBötC burst is concurrent with ∫CNXII activity and iRO oscillation is without. Right, magnified boxed portion showing EPSPs in preBötC inspiratory neurons during iRO expiratory oscillation. **C**, ΔF/F in dozens of iRO neurons (*Snap25*-GCaMP6s), I_c recording preBötC inspiratory neurons with ∫CNXII before (top) and after (bottom) bath application of the iRO rhythm antagonist carbenoxolone. **D**, Left, schematic of the

iRO and preBötC bursting if the two rhythms are coupled or uncoupled. Right, 15 second iRO I_c recording and bottom, average membrane potential ± SD for 125 events aligned to ∫CNXII peak. Action potentials were removed to better visualize membrane potential oscillations. **E**, Left, schematic showing segments measured: blue - intervals between expiratory iRO oscillations, black - last iRO oscillation to preBötC burst. Right, histogram of duration of each segment (black: n = 182 events, blue: n=715 events). Data from 13 mice. **F**, Schematic of iRO induction of post-inspiratory laryngeal adduction (**Figure 2.2**). **G**, Left, examples of iRO (red) and preBötC (black) bursts with associated ∫CNXII activity. iRO activity persists into post-inspiration (Post-I). Right, probability density function showing distribution of burst start and end compared to peak ∫CNXII activity (n = 7 iRO and 12 preBötC neurons). **H**, TA motor neurons identified by intramuscular injection of cholera toxin B-555. Top, example inhibitory post-synaptic currents (IPSCs) in 22/23 motor neurons held at a membrane potential (V_m) of 0 mV. Bottom, example excitatory post-synaptic currents (EPSCs) in 13/22 motor neurons held at -60 mV. Both input types coincide with iRO oscillations and EPSCs are post-inspiratory. **I**, Top, IPSCs are absent in CNQX and APV (V_m, 0 mV). Bottom, post-inspiratory EPSCs are now associated with inspiration in picrotoxin and strychnine (V_m, -60 mV), mirroring iRO activity.

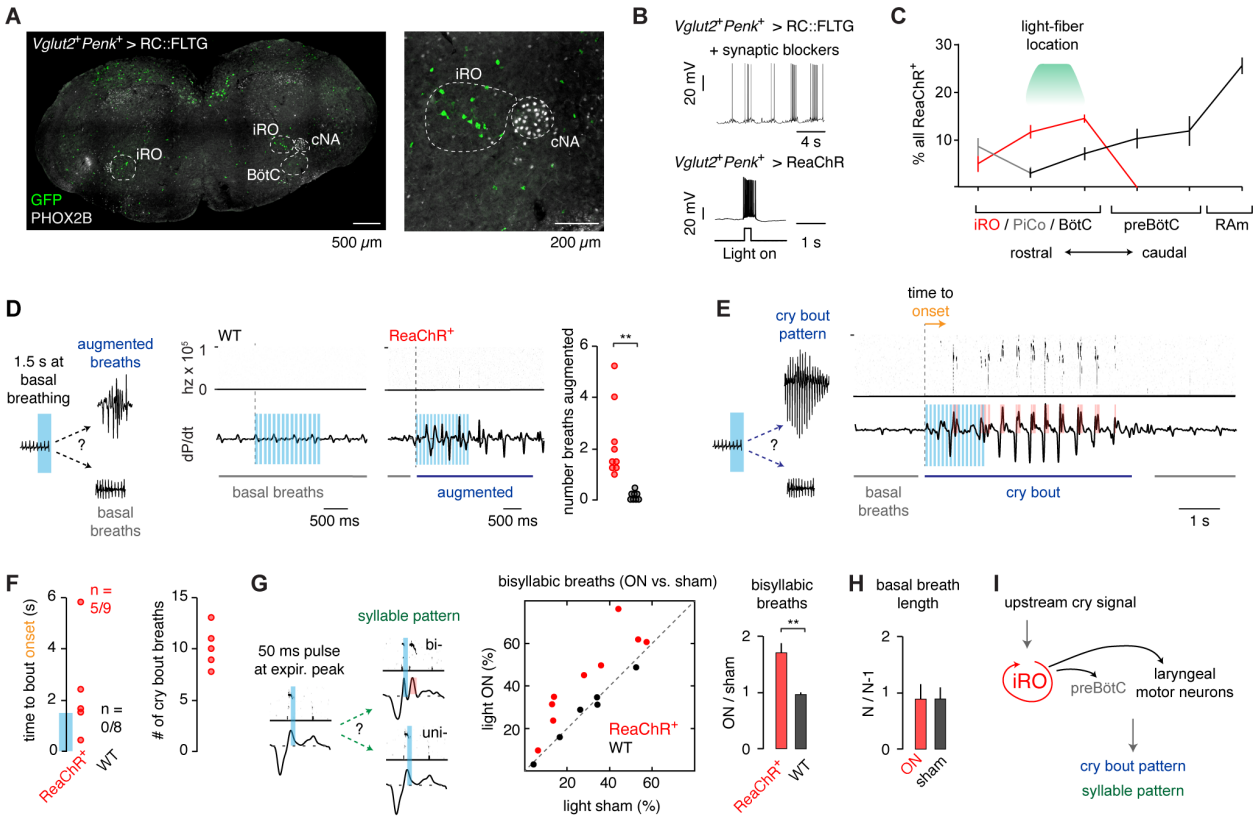

Figure 2.8. The iRO is sufficient to induce neonatal cry bouts and the cry syllables within a breath.

A, Vglut2-Flp; Penk-Cre expression of GFP in the RC::FLTG transgene (Flp + Cre recombination > GFP). 20μm coronal slice of the rostral medullary brainstem showing the distribution of GFP$^+$ neurons (green) and Phox2b expression (gray). Right, magnification of area annotated to outline the iRO, BötC and cNA. Scale bars, 500 and 200μm. **B**, Top, I_c recording of a GFP$^+$ neuron (*Vglut2*$^+$*Penk*$^+$ > GFP) in fast synaptic blockers shows the hallmark iRO rhythm (n = 5/7). Bottom, I_c recording of a ReaChR$^+$ iRO neuron (*Vglut2*$^+$*Penk*$^+$ > ReaChR) with brief light illumination. **C**, Quantification of the proportion of all *Vglut2*$^+$*Penk*$^+$ > ReaChR neurons (percent ± SEM) that localize to the iRO (red), PiCo (gray- ChAT positive), and BötC, preBötC, and RAm (black) (n=3). **D**, Representative change in breathing after 1.5 seconds 10Hz unilateral illumination of the iRO in *Vglut2*$^+$*Penk*$^+$ > ReaChR or wildtype (control) neonatal mice. Average number of augmented breaths in each tested animal (n=9 ReaChR$^+$ and n=8 wildtype). **E**, As in **D**, representative change from basal breathing to a complete cry bout in n=5/9 ReaChR$^+$ animals. **F**, Left, quantification of the time to cry bout onset in ReaChR$^+$ and wildtype neonates. Note, no cry bouts were induced in wildtype neonates. Blue bar on y-axis indicates the duration of laser stimulation. Right, average cry bout length for each ectopically stimulated cry bout in ReaChR$^+$ animal. **G**, Comparison of the percent of cries that show multiple cry syllables or expiratory airflow peaks that accompany each syllable without light (sham, OFF) versus with light (ON) in ReaChR$^+$ and wildtype controls. Right,

mean ± SEM of ON : OFF ratio. **H**, Basal breath length with 50ms opto pulse (N) normalized to the length of the preceding breath (N-1) for breaths with light (ON) and sham. One-sided t-test or Wilcoxon rank sum P-value < 0.01 (**). **I,** Model indicating that the iRO is sufficient to induce the entirety of a cry bout and the syllables that are embedded within it.

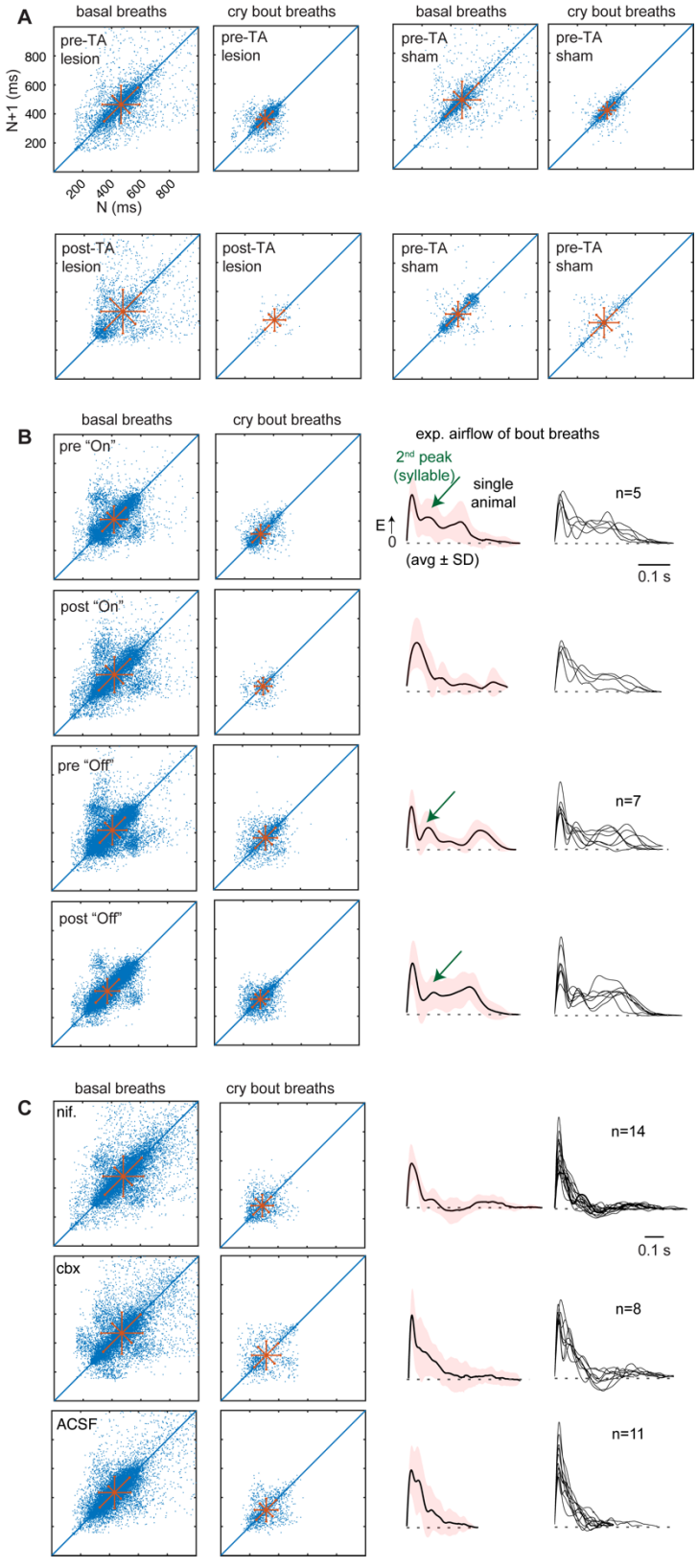
A
basal breaths
cry bout breaths
basal breaths
cry bout breaths
pre-TA lesion
pre-TA lesion
pre-TA sham
pre-TA sham
N+1 (ms)
800
600
400
200
200
400
600
800
N (ms)
post-TA lesion
post-TA lesion
pre-TA sham
pre-TA sham
B
basal breaths
cry bout breaths
exp. airflow of bout breaths
pre "On"
2nd peak (syllable)
single animal
n=5
E
0
(avg ± SD)
0.1 s
post "On"
pre "Off"
n=7
post "Off"
C
basal breaths
cry bout breaths
nif.
n=14
0.1 s
cbx
n=8
ACSF
n=11

Figure 2.9. Characterization of the basal and cry bout breathing rhythms in TA lesions, rv-iRF electrolytic lesions, and rv-iRF pharmacological injections. In reference to Figures 2.2, 2.4, and 2.16.

A, Poincaré plot of breath length (ms) for a breath (N) versus the subsequent breath (N+1) for basal (left) and cry bout (right) breaths before (top) and after (bottom) TA lesion or sham lesion. B, As in A, for breathing before and after on- and off-target electrolytic lesion of the rv-iRF. Right, representative cry breath expiratory airflow (average ± SD) from a single animal and the overlay of the average from all animals. Note, the cry breaths after the post on-target lose the second syllable airflow peak (green arrow). C, As in B, but following pharmacological injection of 10μM nifedipine, 1mM Cbx, or ACSF into the rv-iRF.

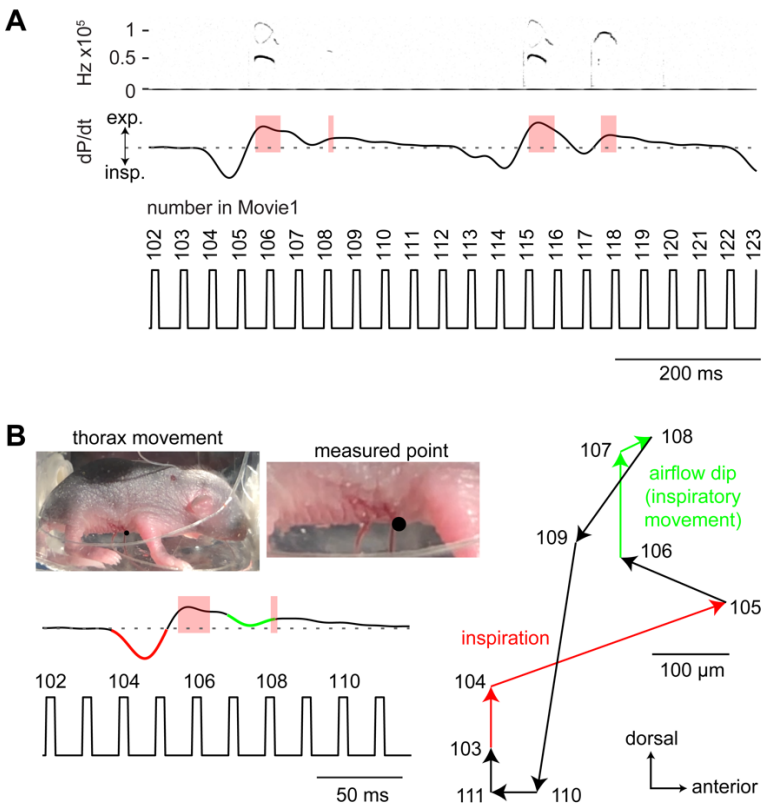

Figure 2.10. Breathing pressure changes and cries that correspond to the breathing movements. In reference to Figure 2.2.

A, Spectrogram and respiratory pressure changes for two sequential breaths with bisyllabic cries. Inspiration occurs in frames 103-105 and 113-115. Inspiratory-like events that separate each syllable occur in frames 106-107 and 116-118. B, Quantification of the thoracic body wall movements. Black dot on the thorax represents the point tracked during the breath. As inspiration occurs, 103-105 (red), the thorax retracted (103-104) and moved anterior (104-105). This same movement, although smaller in magnitude, occurred during the inspiratory like event between the two syllables 106-108 (green). During expiration, the body wall relaxed (108-111). These body wall movements are consistent with the inspiratory motor program measured in Figure 2.2 between syllables and demonstrates that the airflow oscillation between two syllables is likely generated by an inspiratory motor program.

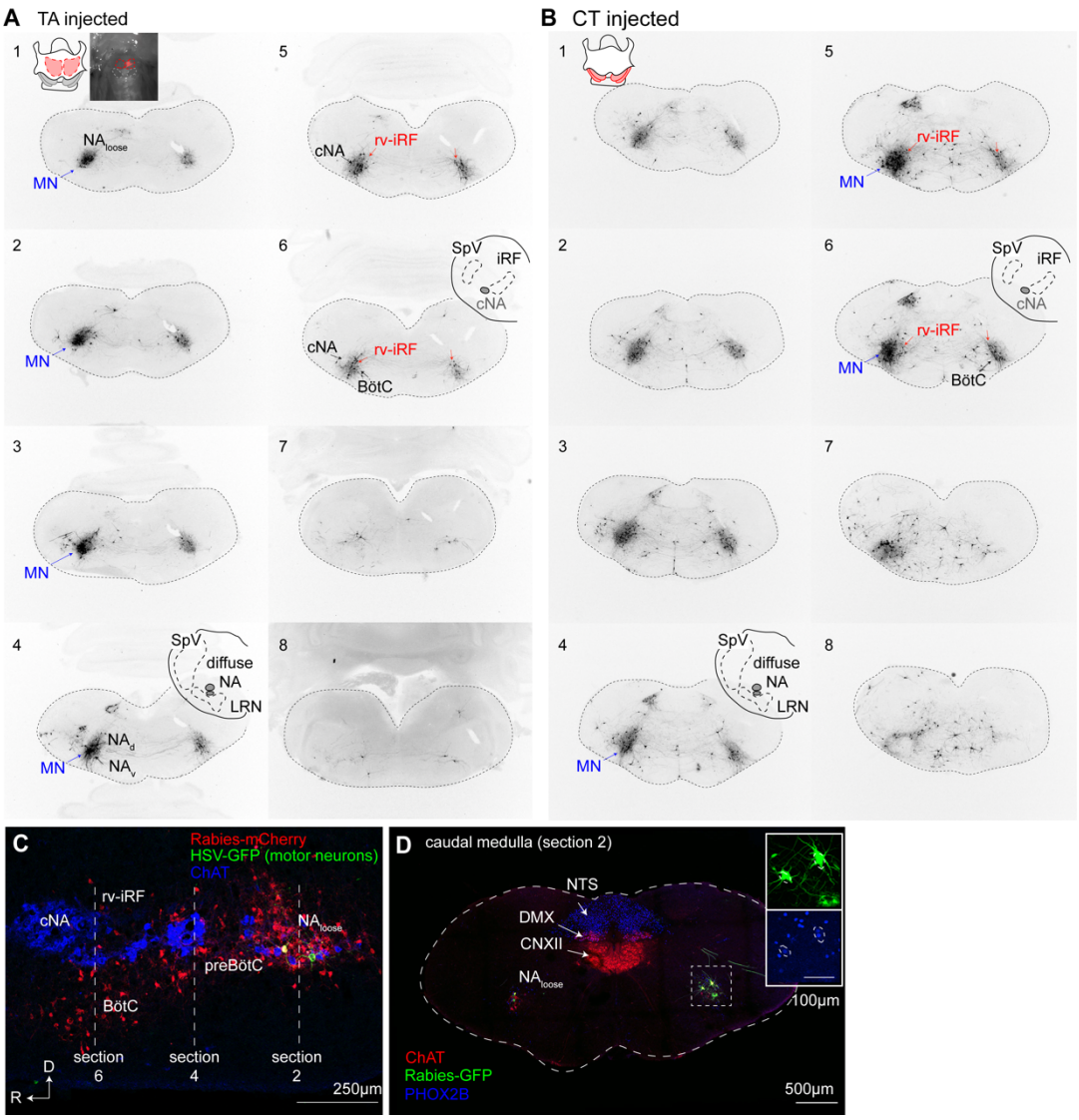

Figure 2.11. Complete medullary motor and premotor pattern from rabies-traced laryngeal muscles. In reference to Figure 2.3.

Sequential coronal sections of the medullary brainstem after ΔG rabies-tracing initiated unilaterally from the thyroarytenoid (TA, **A**) and the cricothyroid (CT, **B**) muscles. Sections are organized from caudal (1) to rostral (8). Red arrows in sections 5 and 6 indicate the anatomical location of rv-iRF. Note, rv-iRF neurons are premotor since they do not express *Phox2b* (**Figure 2.3**). Blue arrows indicate traced motor neurons (MN). These are identified by their large size and *Phox2b* expression (**Figures 2.3** and **2.11**). Furthermore, their locations match the MN patterns identified by HSV-GFP (**Figure 2.12**), the absence of *Vglut2* and *Vgat* expression (**Figure 2.3**), and the literature (Hernández-Morato et al., 2013). Black arrows indicate the loose formation of the nucleus ambiguus (NA_{loose}), semicompact (NA_d and NA_v), and compact (cNA). Black arrows on section 6 also indicate BötC. SpV, Spinal trigeminal nucleus. iRF, intermediate Reticular

Formation. **C**, Sagittal section of the lateral medulla showing TA traced motor neurons after ΔG-rabies-mCherry and HSV-G-GFP microinjection. Motor neurons identified by HSV-Glycoprotein-GFP and *ChAT* expression (green and blue) and ΔG rabies-traced premotor neurons (red, rabies-mCherry positive, HSV-GFP negative, and ChAT negative). TA motor neurons are located in the NA_{loose}. C, caudal. D, dorsal. **D**, Example of coronal brainstem slice showing the thyroarytenoid (TA) motor neurons after ΔG-rabies-GFP microinjection. Motor neurons are identified by colocalization of ΔG rabies-GFP (green) Choline acetyl transferase immunostain (*ChAT*, red), and *Phox2b* immunostain (blue, shown below). Note, the TA motor neurons are in the NA_{loose} in the caudal brainstem where the NTS (nucleus tractus solitarius, *Phox2b* positive), DMX (dorsal motor nucleus 10, *Phox2b* and *ChAT* positive), and CNXII (cranial nerve 12, *ChAT* positive) are located.

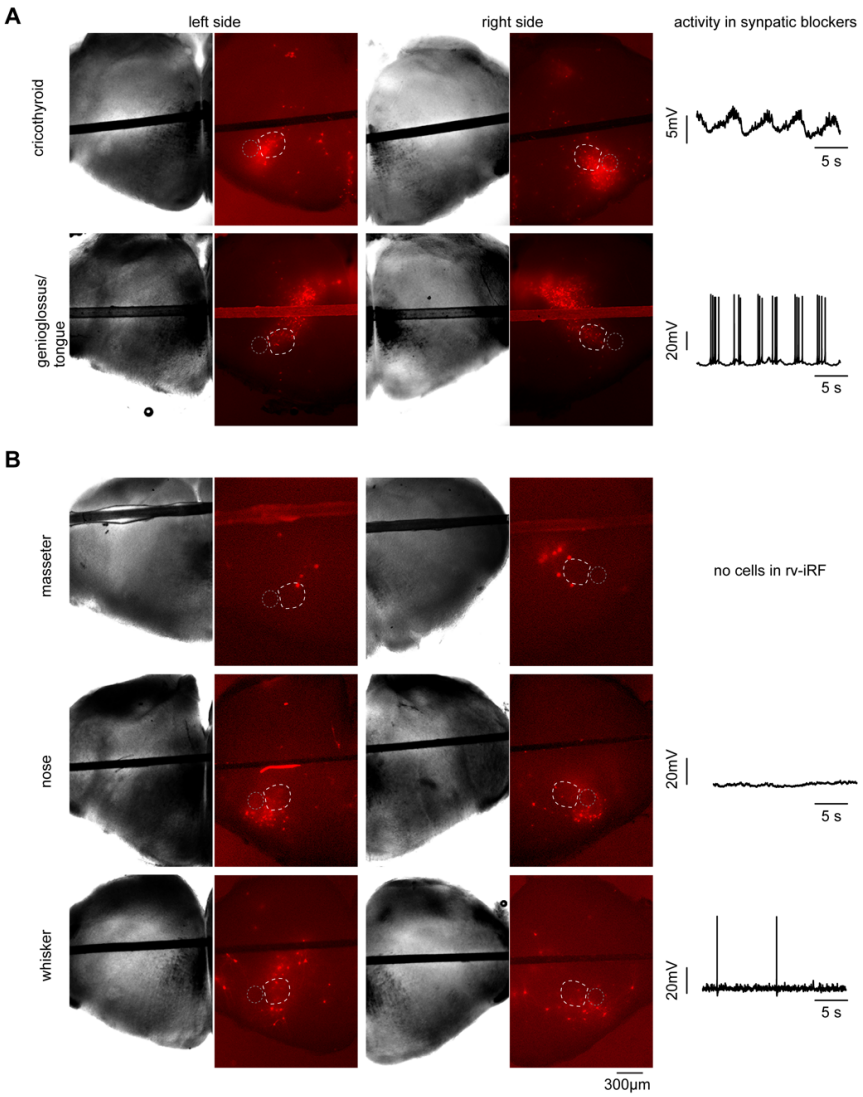

Figure 2.12. Anatomical location of rabies-traced premotor neurons from other orofacial muscles. In reference to Figure 2.3.

A, Left, Corresponding light and fluorescent microscopy images of the left and right sides of medullary brainstem slices depicting the location of the ΔG rabies-mCherry traced motor and premotor neurons (red) after injection of rabies into the cricothyroid and tongue. rv-iRF (dashed white), cNA (dashed gray). Right, Changes in membrane potential measured in current clamp of ΔG rabies neurons in the rv-iRF in fast synaptic neurotransmission (10µM NBQX, 50µM APV, 100µM Picrotoxin, 1µM Strychnine). Oscillation in membrane potential indicates these neurons are within the iRO network (n = 7/19 for CT, n = 5/20 for tongue). **B**, As in A, but ΔG rabies-mCherry injected into other orofacial oscillators. Masseter (chewing, no neurons in rv-IRF), nose (sniffing, n = 0/6), and whisking (whisking, n = 0/5). The few neurons within rv-iRF did not display oscillations in membrane potential. Consistent with the coordination of nose movement and whisking with respiration, some rabies traced neurons localized to the preBötC/BötC, as has previously been described (Kurnikova et al., 2019; Moore et al., 2013; Stanek et al., 2014).

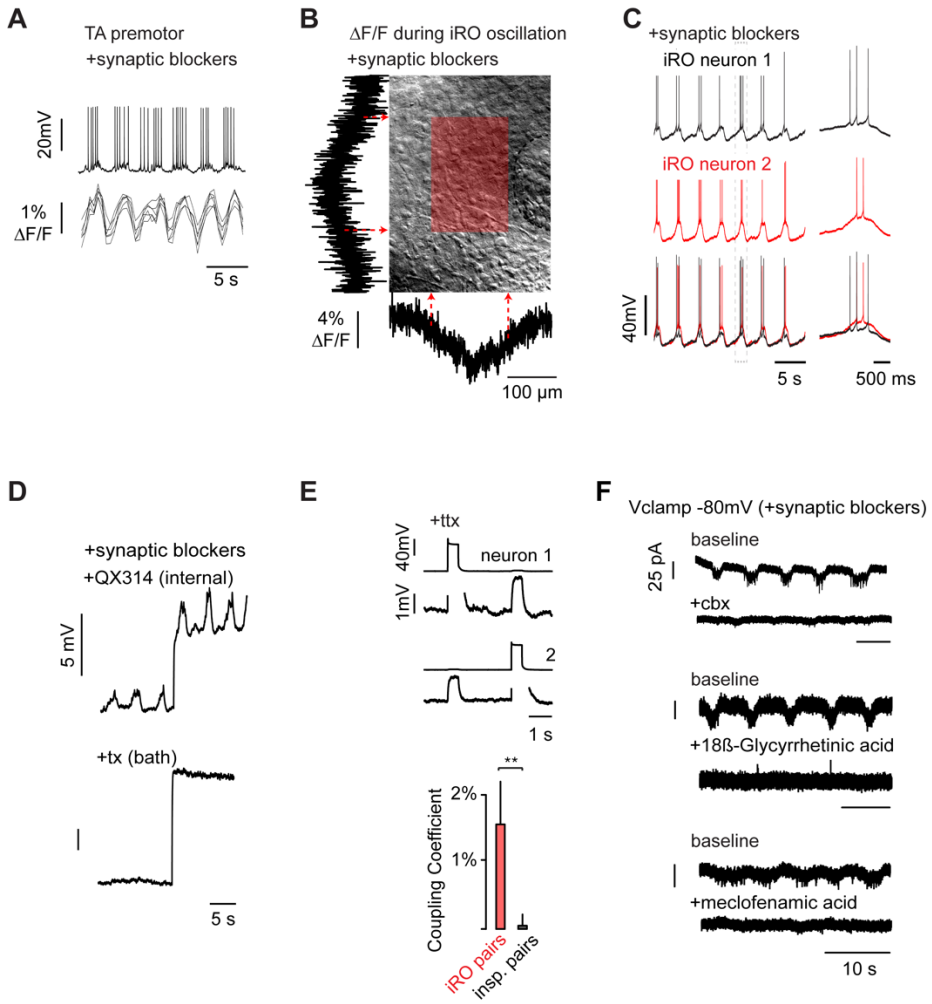

Figure 2.13. Gap junctions are required for the iRO rhythm. In reference to Figure 2.6.

A, I_c recording of TA premotor iRO neuron and ΔF/F in 6 iRO neurons (*Snap25*-GCaMP6s) with bath applied blockers of fast synaptic neurotransmission (10µM NBQX, 50µM APV, 100µM Picrotoxin, 1µM Strychnine). Synchronous rhythmic activity among iRO neurons persists. **B**, ΔF/F summed vertically and horizontally during a single oscillation in synaptic blocker. ΔF/F localizes to only dozens of neurons directly medial to cNA. **C**, Paired current clamp recordings of two iRO neurons in blockers of all fast synaptic neurotransmission (10µM NBQX, 50µM APV, 100µM Picrotoxin, 1µM Strychnine). N = 16. **D**, Current clamp recording in fast synaptic blockers. Top, internal solution with QX314 (5mM). Bottom, same cell after bath application of tetrodotoxin (bottom, 1µM, n = 4). **E**, Paired I_c recordings of iRO neurons in 1µM TTX. 500 picoamp current injection into neuron 1 then neuron 2. Right, Coupling coefficient (ΔmV uninjected / ΔmV injected) for iRO and control inspiratory neuron pairs. iRO coupling coefficient 1.2 ± 1.4%, n = 8; control inspiratory 0.00 ± 0.6%, n = 4. T-test P-value = 0.007. **I**, Voltage clamp recording of iRO neuron at -80 mV with synaptic blockers then with the gap junction antagonists 100 µM carbenoxolone (n = 12), 18ß-glycyrrhetinic acid (150µM, n = 2) and meclofenamic acid (100µM, n = 4).

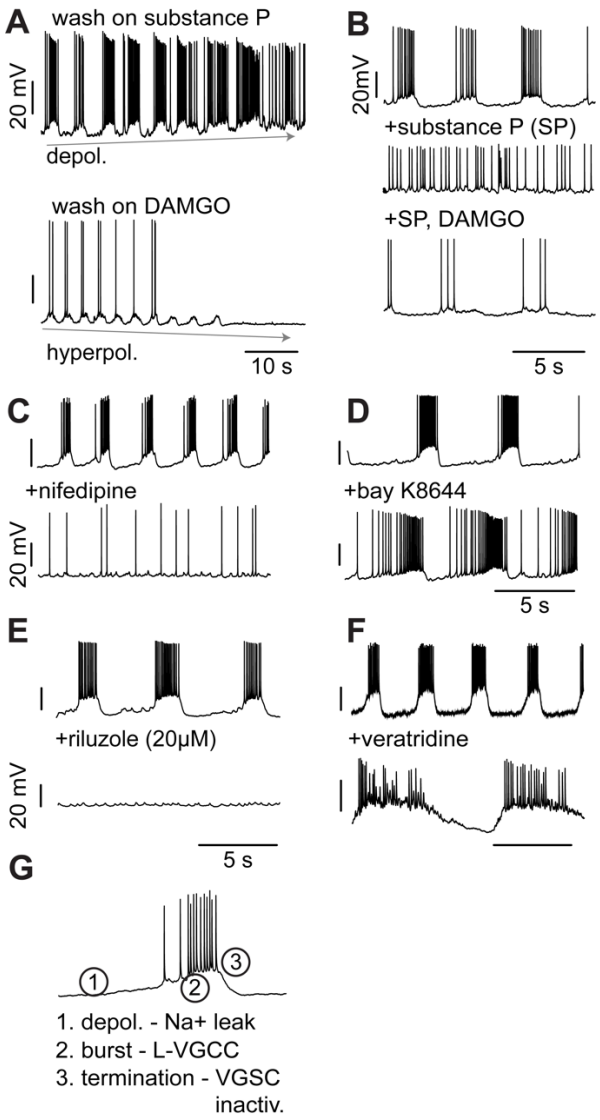

Figure 2.14. The iRO rhythm is voltage dependent. In reference to Figure 2.6.

A, iRO rhythm in fast synaptic blockers during bath application of the depolarizing neuromodulator Substance P (200nM, top) or hyperpolarizing neuromodulator DAMGO (200nM, bottom). **B**, Top, baseline. Middle, Substance P. Bottom, Substance P and DAMGO. **C**-**E**, Current clamp recording iRO neurons in fast synaptic blockers at baseline (top) and after bath application of nifedipine (**C**, 2µM), Bay K8644 (**D**, 100nM), Riluzole (**E**, 20µM), and veratridine (**F**, 250nM). Note, baseline rhythm varies from slice to slice, but each neuron was confirmed to be part of the iRO gap junctioned network based on retained rhythmic activity in fast synaptic blockers. **G**, Model for molecular basis of iRO rhythm. Na^+ leak channels depolarize the network until VGSC spiking occurs (1) which is converted into a burst by L-type voltage gated calcium channels (2). The burst is terminated by inactivation of VGSCs (3).

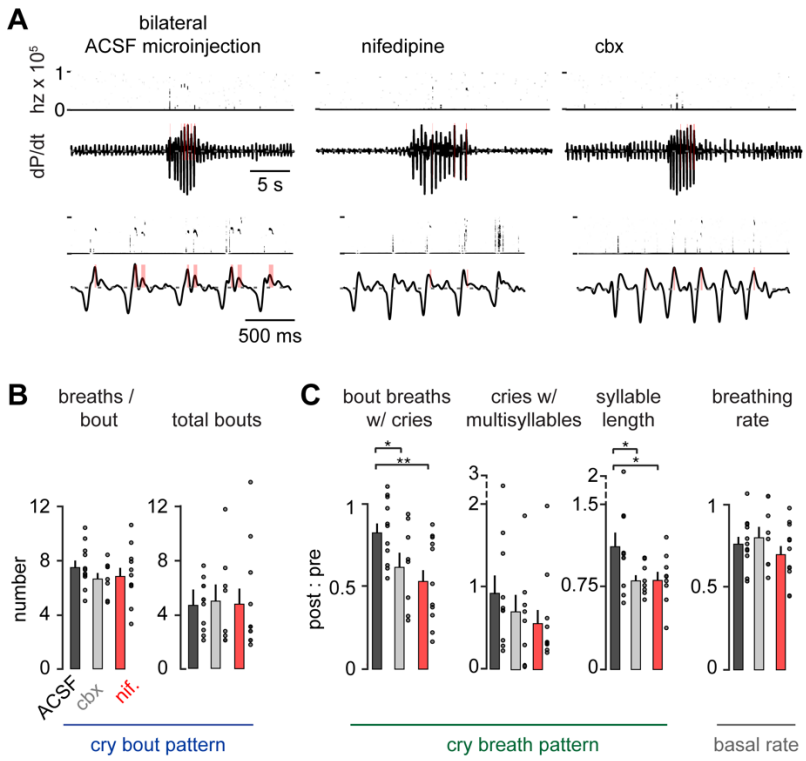

Figure 2.15. The iRO's intrinsic oscillation is required for cries but not breathing. In reference to Figures 2.6 and 2.7.

A, Representative cry bout (top) and breaths within (bottom) after bilateral iRO microinjection of 70nL artificial cerebrospinal fluid (ACSF), 10µM nifedipine, or 1mM Cbx. **B**, Total number of cry bouts and breaths within each bout after microinjection of ACSF (n=11), nifedipine (n=11), or carbenoxolone (n=8). **C**, As in **Figure 2.4**. Post-injection : pre-injection values for the cry breaths with cry vocalizations, multisyllabic cries, cry syllable lengths, and basal breathing. Data are mean ± SEM. One-sided t-test or Wilcoxon rank sum P-value < 0.05 (*) and < 0.01 (**).

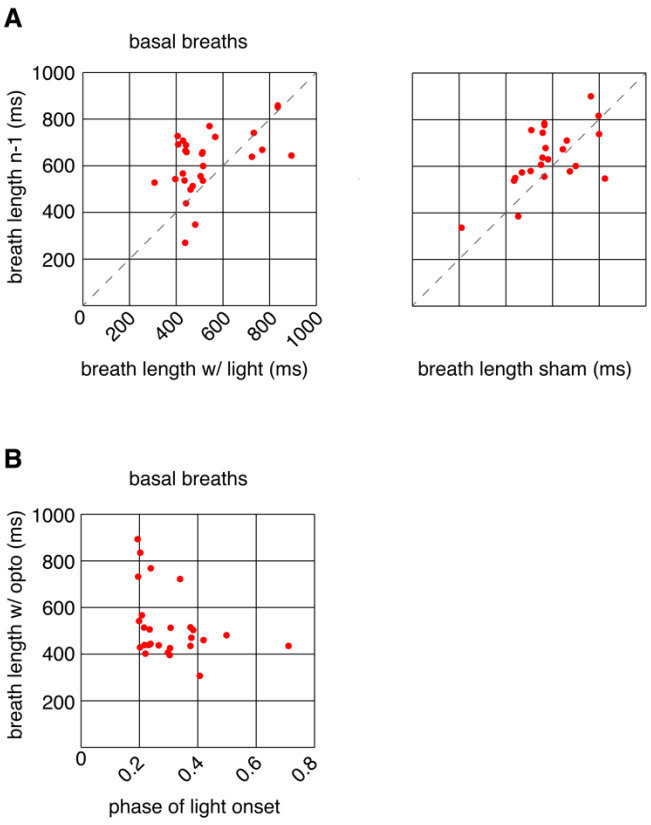

Figure 2.16. The iRO's intrinsic oscillation is required for cries but not breathing. In reference to Figure 2.8.

A, Left, comparison of basal breath rate with 50 ms light stimulation (x-axis, breath w/ light) versus the preceding breath (n-1). Right, sham basal breath versus n-1. **B**, Phase of breath at the onset of the 50 ms pulse (x-axis) versus the breath length. Note that the light pulse does not shift the length of the breath.

TABLE

Table 2.1. iRO activity in transgenic Cre-induced GCaMP6 lines that label different neural types and compartments of the respiratory neural network.

Allele	iRO	Respiratory brainstem compartment	
Vglut2-cre	yes	Glutamatergic	n=4
Gad2-cre	no	Inhibitory	n=4
Vgat-cre	no	Inhibitory	n=3
Glyt2-cre	no	Inhibitory	n=8
RIKEN-Glyt2-cre	no	Inhibitory	n=2
Chat-cre	no	PiCo	n=8
Dbx1-cre	yes	preBötC	n=3
Foxp2-cre	no	preBötC	n=8
Egr2-cre	no	Embryonic parafacial	n=2
Neurod6-cre	no	BötC	n=2
Penk-cre	yes	Neuropeptide	n=1
Parv-cre	no	BötC	n=1
Tac1-cre	yes	Neuropeptide	n=1
NPY-cre	no	A1/C1	n=1

REFERENCES

Anderson, T.M., Garcia, A.J., Baertsch, N.A., Pollak, J., Bloom, J.C., Wei, A.D., Rai, K.G., and Ramirez, J.M. (2016). A novel excitatory network for the control of breathing. Nature *536*, 76–80.

Bielle, F., Griveau, A., Narboux-Nême, N., Vigneau, S., Sigrist, M., Arber, S., Wassef, M., and Pierani, A. (2005). Multiple origins of Cajal-Retzius cells at the borders of the developing pallium. Nature Neuroscience *8*, 1002–1012.

Chagnaud, B.P., Baker, R., and Bass, A.H. (2011). Vocalization frequency and duration are coded in separate hindbrain nuclei. Nature Communications *2*, 346–11.

Daigle, T., Madisen, L., Hage, T., Valley, M., Knoblich, U., Larsen, R., Takeno, M., Huang, L., Gu, H., and Larsen, R. et al. (2018). A Suite of Transgenic Driver and Reporter Mouse Lines with Enhanced Brain-Cell-Type Targeting and Functionality. Cell *174*, 465-480.e22.

Ehret, G. (2005). Infant Rodent Ultrasounds – A Gate to the Understanding of Sound Communication. Behavior Genetics *35*, 19–29.

French, C.R., Sah, P., Buckett, K.J., and Gage, P.W. (1990). A voltage-dependent persistent sodium current in mammalian hippocampal neurons. The Journal of General Physiology *95*, 1139–1157.

Grillner, S., El Marina, A. (2020) Current principles of motor control, with special reference to vertebrate locomotion. Physiological Reviews *100*, 271-320

Hage, S.R. (2009). Localization of the central pattern generator for vocalization. In Handbook of Mammalian Vocalization (Elsevier B.V.), pp. 329-337.

Harris, J.A., Hirokawa, K.E., Sorensen, S.A., Gu, H., Mills, M., Ng, L.L., Bohn, P., Mortrud, M., Ouellette, B., Kidney, J., et al. (2014). Anatomical characterization of Cre driver mice for neural circuit mapping and manipulation. Frontiers in Neural Circuits *8*, 76.

Hernandez-Miranda, L.R., Ruffault, P.L., Bouvier, J.C., Murray, A.J., Morin-Surun, M.P., Zampieri, N., Cholewa-Waclaw, J.B., Ey, E., Brunet, J.F., Champagnat, J., et al. (2017). Genetic identification of a hindbrain nucleus essential for innate vocalization. Proceedings of the National Academy of Sciences of the United States of America *114*, 8095–8100.

Hernández-Morato, I., Pascual-Font, A., Ramírez, C., Matarranz-Echeverría, J., Mchanwell, S., Vázquez, T., Sañudo, J.R., and Valderrama-Canales, F.J. (2013). Somatotopy of the Neurons Innervating the Cricothyroid, Posterior Cricoarytenoid, and Thyroarytenoid Muscles of the Rat's Larynx. The Anatomical Record *296*, 470–479.

Hippenmeyer, S., Vrieseling, E., Sigrist, M., Portmann, T., Laengle, C., Ladle, D.R., and Arber, S. (2005). A Developmental Switch in the Response of DRG Neurons to ETS Transcription Factor Signaling. PLoS Biology *3*, e159-13.

Holy, T.E., and Guo, Z. (2005). Ultrasonic Songs of Male Mice. PLoS Biology *3*, e386-10.

Hooks, B., Lin, J., Guo, C., and Svoboda, K. (2015). Dual-Channel Circuit Mapping Reveals Sensorimotor Convergence in the Primary Motor Cortex. Journal Of Neuroscience *35*, 4418-4426.

Huckstepp, R.T., Henderson, L.E., Cardoza, K.P., and Feldman, J.L. (2016). Interactions between respiratory oscillators in adult rats. ELife *5*, e14203.

Jean, A. (2001). Brain stem control of swallowing: neuronal network and cellular mechanisms. Physiological Reviews *81*, 929–969.

Johnson, A.M., Ciucci, M.R., Russell, J.A., Hammer, M.J., and Connor, N.P. (2010). Ultrasonic output from the excised rat larynx. The Journal of the Acoustical Society of America *128*, EL75–EL79.

Kakizaki, T., Sakagami, H., Sakimura, K., and Yanagawa, Y. (2017). A glycine transporter 2-Cre knock-in mouse line for glycinergic neuron-specific gene manipulation. IBRO Reports *3*, 9–16.

Kam, K., Worrell, J.W., Janczewski, W.A., Cui, Y., and Feldman, J.L. (2013). Distinct inspiratory rhythm and pattern generating mechanisms in the preBötzinger complex. Journal of Neuroscience *33*, 9235–9245.

Kaupp, U.B., and Seifert, R. (2001). Molecular diversity of pacemaker ion channels. Annual Review of Physiology *63*, 235–257.

Kurnikova, A., Deschênes, M., and Kleinfeld, D. (2019). Functional brain stem circuits for control of nose motion. Journal of Neurophysiology *121*, 205–217.

Lim, R., Zavou, M.J., Milton, P.-L., Chan, S.T., Tan, J.L., Dickinson, H., Murphy, S.V., Jenkin, G., and Wallace, E.M. (2014). Measuring respiratory function in mice using unrestrained whole-body plethysmography. Journal of Visualized Experiments : JoVE e51755.

Long, E.C., and Hull, W.E. (1961). Respiratory volume-flow in the crying newborn infant. Pediatrics *27*, 373–377.

Luschei, E.S., Ramig, L.O., Finnegan, E.M., Baker, K.K., and Smith, M.E. (2006). Patterns of laryngeal electromyography and the activity of the respiratory system during spontaneous laughter. Journal of Neurophysiology *96*, 442–450.

Madisen, L., Garner, A.R., Shimaoka, D., Chuong, A.S., Klapoetke, N.C., Li, L., van der Bourg, A., Niino, Y., Egolf, L., Monetti, C., et al. (2015). Transgenic Mice for Intersectional Targeting of Neural Sensors and Effectors with High Specificity and Performance. Neuron *85*, 942–958.

Mahrt, E., Agarwal, A., Perkel, D., Portfors, C., and Elemans, C.P.H. (2016). Mice produce ultrasonic vocalizations by intra-laryngeal planar impinging jets. Current Biology *26*, 1–2.

Marder, E., and Bucher, D. (2001). Central pattern generators and the control of rhythmic movements. Curr Biol *11*, R986–R996.

Milstein, A.D., Bloss, E.B., Apostolides, P.F., Vaidya, S.P., Dilly, G.A., Zemelman, B.V., and Magee, J.C. (2015). Inhibitory Gating of Input Comparison in the CA1 Microcircuit. Neuron *87*, 1274–1289.

Moore, J.D., Deschênes, M., Furuta, T., Huber, D., Smear, M.C., Demers, M., and Kleinfeld, D. (2013). Hierarchy of orofacial rhythms revealed through whisking and breathing. Nature *497*, 205–210.

Mortola, J.P., and Frappell, P.B. (1998). On the barometric method for measurements of ventilation, and its use in small animals. Can J Physiol Pharm *76*, 937–944.

Del Negro, C.A, Funk, G.D., and Feldman, J.L. (2018). Breathing matters. Nature Reviews Neuroscience *254*, 1–17.

Okubo, T.S., Mackevicius, E.L., Payne, H.L., Lynch, G.F., and Fee, M.S. (2015). Growth and splitting of neural sequences in songbird vocal development. Nature *528*, 352–357.

Pagliardini, S., Janczewski, W.A., Tan, W., Dickson, C.T., Deisseroth, K., and Feldman, J.L. (2011). Active Expiration Induced by Excitation of Ventral Medulla in Adult Anesthetized Rats. Journal of Neuroscience *31*, 2895–2905.

Patrickson, J.W., Smith, T.E., and Zhou, S.S. (1991). Motor neurons of the laryngeal nerves. The Anatomical Record *230*, 551–556.

Pattyn, A., Hirsch, M., Goridis, C., and Brunet, J.F. (2000). Control of hindbrain motor neuron differentiation by the homeobox gene Phox2b. Development *127*, 1349–1358.

Plummer, N. W., Evsyukova, I. Y., Robertson, S. D., de Marchena, J., Tucker, C. J., & Jensen, P. (2015). Expanding the power of recombinase-based labeling to uncover cellular diversity. *Development*, *142*(24), 4385–4393.

Poeppel, D., and Assaneo, M.F. (2020). Speech rhythms and their neural foundations. Nature Reviews Neuroscience 1–13.

Pomberger, T., Risueno-Segovia, C., Löschner, J., and Hage, S.R. (2018). Precise Motor Control Enables Rapid Flexibility in Vocal Behavior of Marmoset Monkeys. Current Biology *28*, 788-794.

Prescott, S.L., Umans, B.D., Williams, E.K., Brust, R.D., and Liberles, S.D. (2020). An Airway Protection Program Revealed by Sweeping Genetic Control of Vagal Afferents. Cell *181*, 574-589.

Riede, T. (2014). Rat ultrasonic vocalization shows features of a modular behavior. Journal of Neuroscience *34*, 6874–6878.

Riede, T. (2018). Peripheral Vocal Motor Dynamics and Combinatory Call Complexity of Ultrasonic Vocal Production in Rats (Elsevier B.V.).

Rossi, J., Balthasar, N., Olson, D., Scott, M., Berglund, E., Lee, C.E., Choi, M.J., Lauzon, D., Lowell, B.B., and Elmquist, J.K. (2011). Melanocortin-4 receptors expressed by cholinergic neurons regulate energy balance and glucose homeostasis. Cell Metabolism *13*, 195–204.

Rousso, D.L., Qiao, M., Kagan, R.D., Yamagata, M., Palmiter, R.D., and Sanes, J.R. (2016). Two Pairs of ON and OFF Retinal Ganglion Cells Are Defined by Intersectional Patterns of Transcription Factor Expression. CellReports *15*, 1930–1944.

Ruangkittisakul, A., Kottick, A., Picardo, M.C.D., Ballanyi, K., and Del Negro, C.A. (2014). Identification of the pre-Botzinger complex inspiratory center in calibrated "sandwich" slices from newborn mice with fluorescent Dbx1 interneurons. Physiological Reports *2*, e12111–e12111.

Schwab, M.H., Bartholomae, A., Heimrich, B., Feldmeyer, D., Druffel-Augustin, S., Goebbels, S., Naya, F.J., Zhao, S., Frotscher, M., Tsai, M.J., et al. (2000). Neuronal basic helix-loop-helix proteins (NEX and BETA2/Neuro D) regulate terminal granule cell differentiation in the hippocampus. Journal of Neuroscience *20*, 3714–3724.

Sherman, D., Worrell, J.W., Cui, Y., and Feldman, J.L. (2015). Optogenetic perturbation of preBötzinger complex inhibitory neurons modulates respiratory pattern. Nature Neuroscience *18*, 408–414.

Smith, J.C., Ellenberger, H.H., Ballanyi, K., Richter, D.W., and Feldman, J.L. (1991). Pre-Bötzinger complex: a brainstem region that may generate respiratory rhythm in mammals. Science *254*, 726–729.

Srinivas, S., Watanabe, T., Lin, C.S., William, C.M., Tanabe, Y., Jessell, T.M., and Costantini, F. (2001). Cre reporter strains produced by targeted insertion of EYFP and ECFP into the ROSA26 locus. Bmc Dev Biol *1*, doi:10.1186/1471-213x-1-4.

Stanek, E., Cheng, S., Takatoh, J., Han, B.X., and Wang, F. (2014). Monosynaptic premotor circuit tracing reveals neural substrates for oro-motor coordination. ELife *3*, e02511.

Takatoh, J., Nelson, A., Zhou, X., Bolton, M.M., Ehlers, M.D., Arenkiel, B.R., Mooney, R., and Wang, F. (2013). New modules are added to vibrissal premotor circuitry with the emergence of exploratory whisking. Neuron *77*, 346–360.

Taniguchi, H., He, M., Wu, P., Kim, S., Paik, R., Sugino, K., Kvitsiani, D., Kvitsani, D., Fu, Y., Lu, J., et al. (2011). A resource of Cre driver lines for genetic targeting of GABAergic neurons in cerebral cortex. Neuron *71*, 995–1013.

Tasic, B., Yao, Z., Graybuck, L.T., Smith, K.A., Nguyen, T.N., Bertagnolli, D., Goldy, J., Garren, E., Economo, M.N., Viswanathan, S., et al. (2018). Shared and distinct transcriptomic cell types across neocortical areas. Nature *563*, 72–78.

Titze, I.R., Finnegan, E.M., Laukkanen, A.-M., Fuja, M., and Hoffman, H. (2008). Laryngeal muscle activity in giggle: a damped oscillation model. Journal of Voice *22*, 644–648.

Toor, R.U.A.S., Sun, Q.J., Kumar, N.N., Le, S., Hildreth, C.M., Phillips, J.K., and McMullan, S. (2019). Neurons in the Intermediate Reticular Nucleus Coordinate Postinspiratory Activity, Swallowing, and Respiratory-Sympathetic Coupling in the Rat. Journal of Neuroscience *39*, 9757–9766.

Tschida, K., Michael, V., Takato, J., Han, B.-X., Zhao, S., Sakurai, K., Mooney, R., and Wang, F. (2019). A Specialized Neural Circuit Gates Social Vocalizations in the Mouse. Neuron *103*, 459-472.

Voiculescu, O., Charnay, P., and Schneider-Maunoury, S. (2000). Expression pattern of a Krox-20/Cre knock-in allele in the developing hindbrain, bones, and peripheral nervous system. Genesis *26*, 123–126.

Vong, L., Ye, C., Yang, Z., Choi, B., Chua, S., and Lowell, B.B. (2011). Leptin action on GABAergic neurons prevents obesity and reduces inhibitory tone to POMC neurons. Neuron *71*, 142–154.

Wilder, C.N. (1974). Respiratory patterns in infant cry. Human Communication Winter 18–34.

Yamanishi, T., Koizumi, H., Navarro, M.A., Milescu, L.S., and Smith, J.C. (2018). Kinetic properties of persistent Na^+ current orchestrate oscillatory bursting in respiratory neurons. The Journal of General Physiology *150*, 1523–1540.

Zhang, Y.S., and Ghazanfar, A.A. (2020). A Hierarchy of Autonomous Systems for Vocal Production. Trends in Neurosciences *43*, 1–12.

CHAPTER 3: FUTURE DIRECTIONS

Role of the iRO in vocalizations of adult mouse and other species

It will be important to determine whether the iRO's role in timing syllable onset is generalizable to adult mouse vocalizations, as well as those of different species, and how this is utilized or bypassed during learned vocalizations or song. It is possible that more complex and diverse syllables, like that in human speech, results from learned fine motor control of the articulator muscles, but the rhythmic timing of sounds production remains patterned by innate iRO oscillations. Our identification of a molecular signature of iRO neurons (*Vglut2*$^{+}$*Penk*$^{+}$) will provide one avenue to investigate its role in adult vocalizations in mice and perhaps other species.

Disruptions to the iRO may have clinical implications.

Hardwired patterning systems like the iRO allow the brain to generate robust, reproducible motor tasks that are essential for innate behaviors, such as crying. Improper development or execution of the precise motor sequence encoded by the iRO may lead to significant communication deficits. Indeed, we show that neonatal mice with disrupted iRO activity fail to properly pattern vocalizations. Thus, this study opens a new possibility that patients with motor speech disorders, particularly those affected by mutism or oromotor dyspraxia, may have defects in the iRO or neural circuits connected to the iRO.

Might iRO be re-purposed for other behaviors?

Because the iRO can coordinate breathing with laryngeal adduction, we imagine that it may be repurposed for non-vocalization behaviors that also require laryngeal closure, including

spontaneous laughter (Luschei et al., 2006; Titze et al., 2008) and swallowing (Jean, 2001; Prescott et al., 2020; Toor et al., 2019). Indeed, neurons within the anatomical region of the iRO have previously been implicated in swallowing (Toor et al., 2019). Both its restricted anatomical location and rhythmic activity make the iRO an ideal system for studying the role of higher brain centers and neuromodulation in sculpting or repurposing a pattern generating system to support a range of both innate and learned mammalian behaviors.

REFERENCES

Jean, A. (2001). Brain stem control of swallowing: neuronal network and cellular mechanisms. Physiological Reviews *81*, 929–969.

Luschei, E.S., Ramig, L.O., Finnegan, E.M., Baker, K.K., and Smith, M.E. (2006). Patterns of laryngeal electromyography and the activity of the respiratory system during spontaneous laughter. Journal of Neurophysiology *96*, 442–450.

Prescott, S.L., Umans, B.D., Williams, E.K., Brust, R.D., and Liberles, S.D. (2020). An Airway Protection Program Revealed by Sweeping Genetic Control of Vagal Afferents. Cell *181*, 574-589.

Titze, I.R., Finnegan, E.M., Laukkanen, A.-M., Fuja, M., and Hoffman, H. (2008). Laryngeal muscle activity in giggle: a damped oscillation model. Journal of Voice *22*, 644–648.

Toor, R.U.A.S., Sun, Q.J., Kumar, N.N., Le, S., Hildreth, C.M., Phillips, J.K., and McMullan, S. (2019). Neurons in the Intermediate Reticular Nucleus Coordinate Postinspiratory Activity, Swallowing, and Respiratory-Sympathetic Coupling in the Rat. Journal of Neuroscience *39*, 9757–9766.

Publishing Agreement

It is the policy of the University to encourage open access and broad distribution of all theses, dissertations, and manuscripts. The Graduate Division will facilitate the distribution of UCSF theses, dissertations, and manuscripts to the UCSF Library for open access and distribution. UCSF will make such theses, dissertations, and manuscripts accessible to the public and will take reasonable steps to preserve these works in perpetuity.

I hereby grant the non-exclusive, perpetual right to The Regents of the University of California to reproduce, publicly display, distribute, preserve, and publish copies of my thesis, dissertation, or manuscript in any form or media, now existing or later derived, including access online for teaching, research, and public service purposes.

DocuSigned by:
Paul Wei
E1CA528A182D40B...
Author Signature

12/7/2021
Date